Chapter 5

A Catalog of Large H I Shells in the Southern Galactic Plane Survey

Abstract

In this chapter we present new H I shells from the Southern Galactic Plane Survey (SGPS). We have discovered nineteen new shells ranging in radius from 100 pc to 1 kpc. We discuss the properties of the individual shells, including positions, physical dimensions, energetics, masses, and possible associations. Radius and expansion velocity distributions for shells in the Milky Way are examined and compared to external galaxies: M31, M33, Holmberg II, the Large and Small Magellanic Clouds. Finally we discuss, with specific examples, what may be gained from high resolution observations of H I shells, such as those using the complete SGPS data.

5.1 Introduction

The majority of known H I shells were cataloged in surveys of the Northern sky (e.g. Heiles 1984, 1979). The Southern Galactic Plane, with its view of the inner Galaxy, has not been carefully studied. Star formation rates are expected to be highest in the inner Galaxy and therefore the number of shells should be highest there. Varying selection criteria have led to a catalog that contains many shell types, and possibly objects that are not shells, including those with noticeable velocity structure and those that are simply arcs of emission at a given velocity. This chapter is motivated by the need for a complete catalog to investigate shell properties and evolution. A thorough, complete sample is needed before we can attempt to classify shell types, formation mechanisms, and distributions. It has been noted that some shells are very energetic, apparently requiring in excess of 10^{53} ergs of formation energy. However, with the relatively small sample of of known shells in the Milky Way it is difficult to determine which formation mechanisms are at work. Because of the incomplete Galactic sample, our knowledge of the impact of shells on the Milky Way is limited.

In this chapter we present a thorough catalog of large H I shells in the SGPS. We discuss their individual and global properties. In section 5.2 we describe the selection criteria, biases and methods for determining shell properties. In section 5.3 we present the shells that are not described elsewhere in this work. We briefly discuss the general properties of H I shells in the Milky Way in section 5.4. Finally, in section 5.5 we address what may be learned from studying shells at high resolution, such as with the full SGPS, and examine several shells in this context.

5.2 Identifying New H I Shells

We have discovered nineteen new large H I shells in the SGPS data. This sample includes only shells of angular size one degree or larger. The shells were identified by eye (i.e. without automated searching algorithms) in the Parkes data cubes (resolution $16'$). H I shell candidates must meet three criteria to be included in the catalog. Those criteria are:

- Shells are first identified as roughly elliptical, clearly defined voids in the H I channel images. The void must be observed over at least four consecutive channels ($\Delta v \sim 4$ km s^{-1}) to be considered as a shell, rather than a filament. These voids are also characterized by a shell wall to shell interior brightness temperature contrast of a factor of five or more.

- Shell candidates must change in size with LSR velocity. This characteristic implies that the shell is a three-dimensional structure and not simply an arc or filament. An ideal spherical, expanding shell would appear as a series of rings in consecutive H I channel images. These rings decrease in size away from the shell's center, culminating in a small disk - or cap - at the velocity extremes of the shell. Though none of the shells presented here are ideal, expanding spheres, all shells change angular radius in consecutive channel images.

- Velocity profiles through the apparent centers of shell candidates are extracted. A true shell is readily identified by a dip in the velocity profile, flanked by peaks (examples are shown in Figs. 5.1-5.15). The dip is the H I void itself and the flanking peaks are the two caps of the expanding shell. The minimum of the velocity profile is identified with the center of the shell, which is also usually the velocity at which the shell attains its greatest angular size.

If a putative shell meets all three criteria it is given a confidence rating of 1 and added to the catalog. Shell candidates that meet two criteria have a confidence rating of 0.66 and those meeting only one criteria have a confidence rating of 0.33. The latter two categories are not included in the catalog.

It is imperative that spectra demonstrating a shell-like bowl be compared with spectra from positions adjacent to the shell. H I spectra in the Galaxy are complicated, in addition to shells, dips in the spectrum may be due to absorption by cold gas or decreases in emission due to regions between spiral arms, among other things. Distinguishing between interarm regions and H I shells can largely be accomplished by examining spectra taken adjacent to the shell. If these spectra do not show a similar dip in the profile then the decreased emission is likely due to a shell or absorption. Distinguishing between absorption and a shell, however, is more difficult. In both cases the dip in the profile is localized to the region identified as a void in the channel images. Minter et al. (2001) note, though, that a shell can be distinguished from self-absorption by the subtle details of the velocity profile. Self-absorption typically has a narrower width with steeper walls. Random cloud motions will blur and broaden the edges of an emission profile bowl due to a shell, whereas a self-absorption feature will not be as broad. Finally, the relatively small change in velocity with distance throughout most of the Galaxy means that cold clouds of a finite size will have narrow velocity widths. By contrast, the velocity width of a shell is determined by its expansion velocity and is therefore much broader.

5.2.1 Selection Biases

Identifying shells by eye is a subjective process and results in a number of biases in the compiled catalog. The stringent selection criteria employed here differ from those used for the Heiles (1979, 1984) catalogs. These criteria severely limit the number of shells included in the catalog. Those that are included, however, are at a high confidence level. There are, though, many shell-like structures that do not meet all criteria and were therefore not included in the catalog. Based on the ratio of the number of shell-like objects to cataloged shells in select fields in the outer Galaxy we estimate that shell-like objects with confidence ratings of 0.66 outnumber cataloged shells by a factor of 2 to

1. In the inner Galaxy this ratio is increased to about 3 to 1 due to the number of potential shells whose velocity profiles do not demonstrate the requisite bowl. Because the structure of the H I in the outer Galaxy can largely be characterized as filamentary it is impossible to estimate the number of filaments, or objects of confidence 0.33, that might be portions of shells. In total, though, we believe there may be a further ~ 50 large H I shells that have not been cataloged here. Comparison with the surveys of the Large and Small Magellanic Clouds (Kim 1998; Stanimirović et al. 1999) would lead us to expect more, however.

The number of shells found in the outer Galaxy outnumbers those in the inner Galaxy by almost a factor of four. Shells in the outer Galaxy are considerably easier to detect than those in the inner Galaxy. The distance ambiguity results in a much higher filling factor for H I emission at all inner Galaxy velocities. Objects that might otherwise appear as voids are filled by emission from another Galactic position. This selection bias is further worsened by the criterion that shells exhibit the characteristic bowl in the velocity profile. Possible shells in the inner Galaxy often do not have a definitive dip in the velocity profile. Because lower longitudes ($l < 310^\circ$) cover more of the outer Galaxy at comparatively nearby distances, shells are easier to detect at low longitudes. Lines of sight at high longitudes ($l > 340^\circ$) largely cover the inner Galaxy (negative velocities), positive velocities are at large distances, making outer Galaxy shells difficult to detect both because of their small angular size and weak emission.

The cubes used to identify shells cover $16^\circ \times 22^\circ$ each. This leads to a bias towards selecting shells that are several degrees in angular scale. Examinations of sub-cubes are required to find smaller shells. These, however, are often lost in the complicated small scale structure. Similarly, extremely large angular diameter shells, those larger than tens of degrees, may extend beyond the edge of the cubes and therefore escape detection. The two extremely large angular diameter shells included in the catalog are very continuous and therefore straightforward to detect.

Finally, many discovered shells are located at the edge of spiral arms, which we believe may be partially a selection effect and partially a true distribution. (See Chapter 8 for a discussion of the Galactic distribution of H I shells.) However, it should be noted that H I shells at the edge of spiral arms are easier to detect than those in arms. One reason is that, as noted in Chapter 3 with regard to GSH 277+00+36 and GSH 280+00+59, a shell expanding into an interarm region can grow slightly larger than one expanding into a constant ambient density and it is easier to detect. Additionally, the interarm region will increase the depth of the velocity profile, making these shells easier to identify by their profile. And finally, there is less emission in the interarm regions and therefore less confusion.

It is difficult to overcome selection biases in H I shell catalogs. An obvious solution would be to apply an automated searching algorithm. Several attempts have been made to create automated searching routines for H I shell identification (e.g. Thilker et al. 1998). The Thilker et al. (1998) technique is based on three-dimensional cross correlation between a simulated pattern and real data. While this technique seems to be effective in external galaxies, attempts to apply the technique to the Milky Way have not proven successful. The rapidly varying rotation curve, coupled with the often non-spherical shell shape and the intertwined nature of many shells, makes it difficult to apply an automated technique that expects a shell to agree with models. Mashchenko et al. (1999) have attempted to overcome this limitation by elaborating on three-dimensional hydrodynamical simulations of shells to include more realistic models. This technique has been applied with moderate success in Canadian Galactic Plane Survey (CGPS) data (Mashchenko et al. 1999). However, the application has been limited to shells around single stars for which the physics is considerably more simple than for supershells. We have yet to see a successful application of automated techniques to large shells in the Galaxy.

5.2.2 Determining Shell Properties

Here we discuss the techniques used to determine observed and derived parameters for all shells including: physical dimensions, expansion velocity, formation energy, swept-up mass, and column density. The observed parameters are listed in Table 5.1 and derived parameters are given in Table 5.2. The center of the shell in galactic longitude, latitude, and velocity is the point of the least emission nearest to the apparent geometric center. In all cases this center agrees to within $30'$ and 6 km s^{-1} with the geometric center. Kinematic shell distances and physical sizes are estimated from the shell's center velocity, using the rotation curve of Fich et al. (1989), and the angular diameters of the major and minor axes of the shell. We adopt the IAU standard values for the Sun's orbital velocity, $\Theta_o = 220$ km s^{-1} and Galactic center distance, $R_o = 8.5$ kpc. Error estimates for distance determinations are based on the assumption that departures from Galactic circular rotation due to streaming motions can be as high as $\sim$ 10 km s^{-1} (Burton 1988), and therefore the distances derived from the rotation curve will have associated uncertainties. To estimate the mass swept-up by the expanding shell we calculate the column density through the center of the shell, including the entire void and both caps. We then use the average as a representative number for the shell, assuming that the column density in the void is negligible. The error is based on the standard deviation of the mean in the shell center. If we assume that the majority of the mass in the shell caps comes from the interior we can use the column density to estimate the ambient density of the medium into which the shell expanded. We assume a spherical geometry for the shell, using the radius in the plane as the characteristic radius because assumption of a constant ambient density is more applicable along the plane than perpendicular to it. We then calculate the swept-up mass from the shell volume and ambient gas density. The errors in column density and those in radius propagate through to the ambient density and swept-up mass.

The expansion velocity is estimated as half of the total velocity width of the shell.

This is most easily determined from the velocity profile through the center of the shell. Using the peaks on either side of the shell bowl, we determine a full velocity width for each shell. Separating the expansion velocity from the spatial extent of the shell is difficult. For each shell we calculate the velocity gradient along the line of sight and compare the observed velocity width of the shell to the inferred velocity width due to the spatial extent of the shell. In order to do this we assume that the shell is nearly spherical and then calculate the expected velocity width from the velocity gradient. In all cases the velocity spread due only to the spatial extent of the shell is less than 20% of the observed shell velocity width. We therefore assume that the observed width is due to expansion and estimate that, to first order, the expansion velocity is half of the full velocity width, $v_{\rm exp} \approx \Delta v/2$.

The dynamic age, an estimate of the age based on the dynamic properties of the shell, is calculated from the standard Weaver et al. (1977) analytic solutions for an expanding wind bubble. These equations assume a thin-shell with a continuous energy injection rate. Mac Low & McCray (1988) found that for simulated shells, a continuous energy injection was adequate. In Chapter 4 we also found that shell properties varied little for a continuous energy injection versus an energy injection that increases as a step-function. So, following Weaver et al. (1977) and Mac Low & McCray (1988) the time evolution of the radius and velocity of a supershell can be written as

$$R_{sh} = (66 \text{ pc})\ L_{38}^{1/5} n_0^{-1/5} t_6^{3/5} \tag{5.1}$$

$$v_{\rm exp} = (39 \text{ km s}^{-1})\ L_{38}^{1/5} n_0^{-1/5} t_6^{-2/5}, \tag{5.2}$$

where L_{38} is the input wind luminosity in units of 10^{38} ergs s^{-1}, t_6 is the shell dynamic age in units of 10^6 yrs, and n_0 is the ambient ISM number density in units of cm^{-3}. Solving for t_6, the dynamic age of the shell is

$$t_6 = \frac{13}{22}\ \frac{R_{sh}}{v_{exp}}. \tag{5.3}$$

We use the expansion velocity and shell radius to estimate the shell's expansion energy, E_E. As defined by Heiles (1984), the expansion energy is the equivalent energy instantaneously deposited at the shell center to account for the shell's radius, $R_{\rm sh}$ and current rate of expansion, $v_{\rm exp}$. Based on the Chevalier (1974) calculations for supernova remnant expansion, the expansion energy is given by $E_E = 5.3 \times 10^{43}\, n_0^{1.12}\, R_{\rm sh}^{3.12}\, v_{\rm exp}^{1.4}$ ergs. We note that the expansion energy is strongly dependent on the shell radius, and that for a large shell with a non-zero expansion velocity the required formation energies can be very large $\sim 10^{53}$ ergs.

5.3 Discussion of Individual Shells

Below we present images of the newly cataloged shells and discuss their individual properties. For each shell a grey scale image at the central velocity is shown in the top panel. In the bottom panel the velocity profile through the center of the shell is shown with the rotation curve along the line of sight. Four shells: GSH 277+0+37, GSH 280+0+59, GSH 304+01-24, and GSH 305-00-12 are included in the catalog but not shown here because they were previously discussed in Chapters 3 & 4.

5.3.1 GSH 255-00+52

GSH 255-00+52, as shown in Fig. 5.1, is centered at $l = 255\overset{\circ}{.}19$, $b = -0\overset{\circ}{.}49$, $v = +52$ km s^{-1}. The shell walls are diffuse, but there is a clear shell signature in the velocity profile and a distinct void in the image plane that changes size with velocity. The shell extends over $3\overset{\circ}{.}8$ in longitude and $3\overset{\circ}{.}7$ in latitude. The central velocity indicates a distance of 5.3 kpc, which implies major axes of 350 pc and 340 pc in l and b, respectively. The velocity profile suggests an expansion velocity of $v_{exp} \sim 18$ km s^{-1}. We calculate an ambient density of $n_0 \approx 1.7$ cm^{-3} and a swept-up mass of 1.3×10^6 M$_\odot$. The radius, ambient density and expansion velocity give an expansion energy of $E_E \sim 5.3 \times 10^{52}$ ergs.

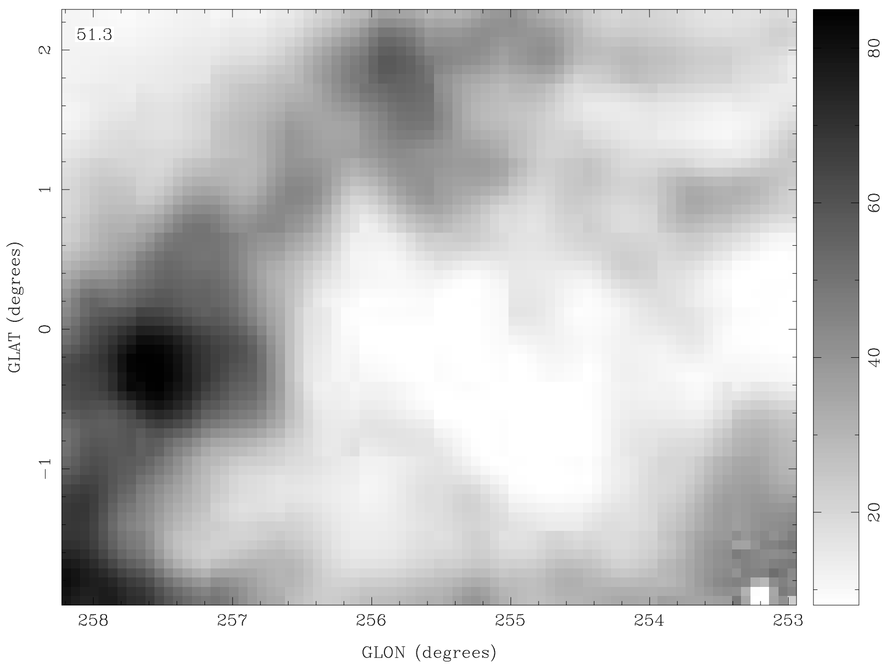

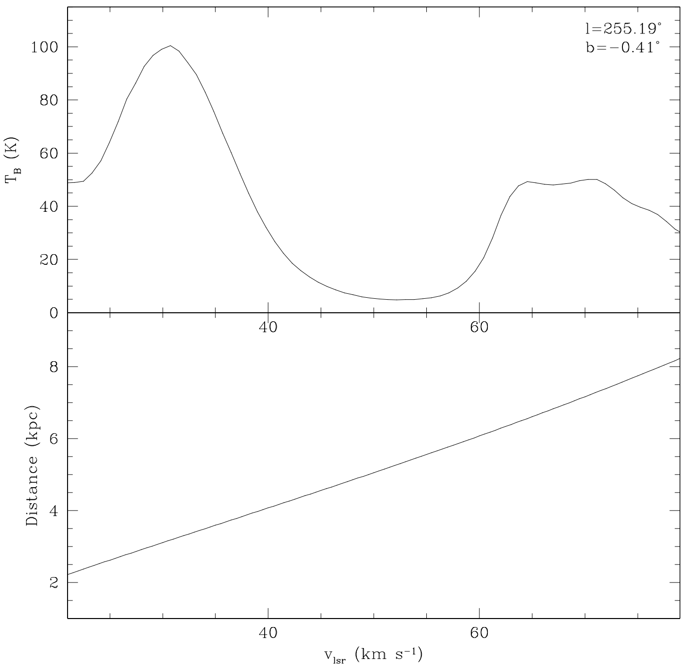

Figure 5.1: Grey-scale image of GSH 255-00+52 (top) and velocity profile through the shell, with the corresponding rotation curve along the line of sight (bottom). The grey-scale is linear in brightness temperature as shown on the wedge at the right.

5.3.2 GSH 256+00+63

GSH 256+00+63 is centered at $l = 256\overset{\circ}{.}59$, $b = -0\overset{\circ}{.}142$, $v = +63$ km s^{-1}. Fig. 5.2 is a grey-scale image of the shell at $v = 62.9$ km s^{-1} and the velocity profile through the shell. The shell is nearly circular, has distinctive brightened edges and opens at both the top and bottom edges. The near and far caps are detected at $v = 49$ km s^{-1} and $v = 74$ km s^{-1}, respectively. There is a faint, narrow (unresolved in b) filament that extends across the shell from $l = 255\overset{\circ}{.}4$ to $l = 256\overset{\circ}{.}9$ at the central velocity. The brightness temperature contrast between the edge of the shell and the middle is a factor ~ 8.

The central velocity places the shell at a distance of 6.5 kpc, and implies a physical radius of ~ 145 pc. On the right edge of the shell at $l = 254\overset{\circ}{.}67$, $b = +0\overset{\circ}{.}22$ there is an H II region with a recombination velocity of $v = +64$ km s^{-1} (Caswell & Haynes 1987). The relationship between the shell and H II region is explored in section 5.5.2. The expansion velocity is ~ 12 km s^{-1}. We calculate an ambient density of $n_0 \approx 1.0$ cm^{-3} and a swept-up mass of 4.2×10^5 M$_\odot$. Therefore, the shell has an expansion energy of $\sim 9 \times 10^{51}$ ergs.

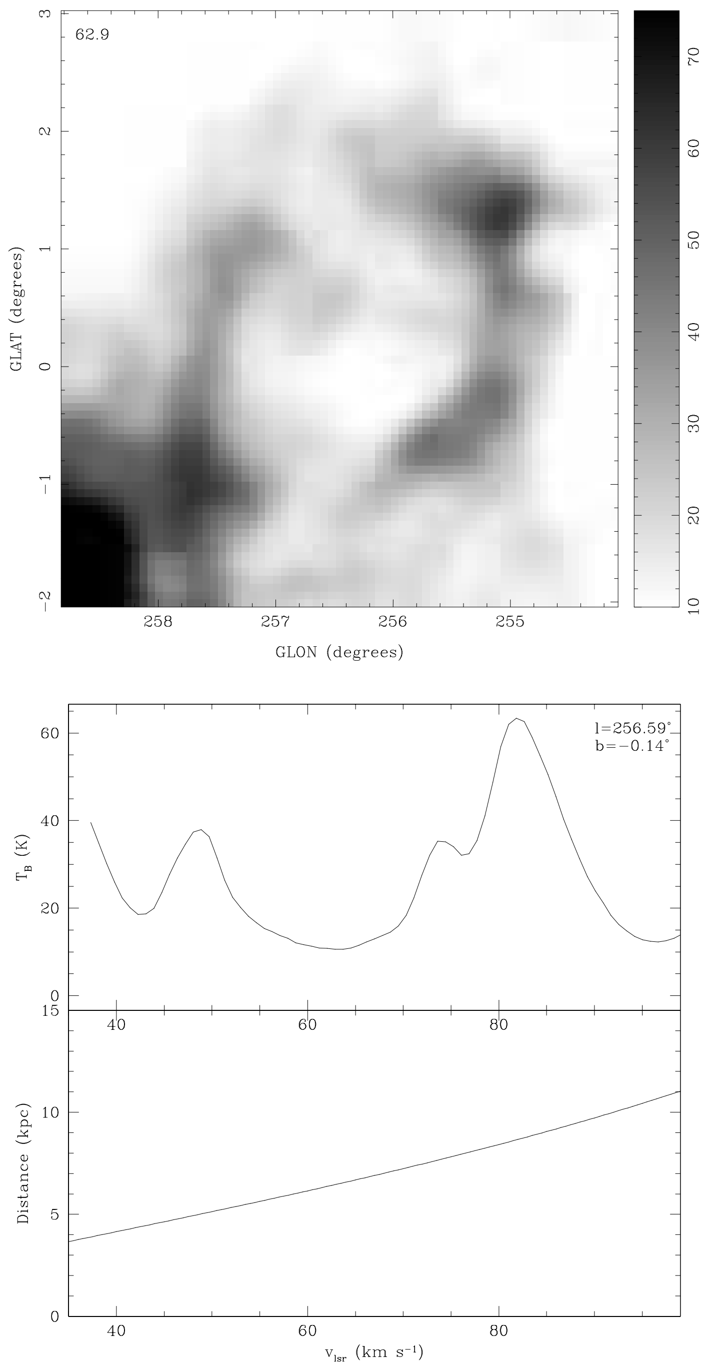

Figure 5.2: Grey-scale image of GSH 256+00+63 (top) and velocity profile through the shell, with the corresponding rotation curve along the line of sight (bottom). The grey-scale is linear in brightness temperature, as shown on the wedge at the right.

5.3.3 GSH 263+00+47

GSH 263+00+47, as shown in Figure 5.3, is distinguished by its irregular shape. The morphology is very unusual; there is a central, empty region with a typical brightness temperature of only ~ 5 K. Surrounding this region there are filaments that seem to delineate two smaller shells that have merged to create one, large shell. Each of these two apparent sub-shells is formed by nearly completely looped filaments with angular diameters of $\sim 1^\circ$ each. The full shell has an angular diameter of $5\overset{\circ}{.}1$ in longitude and 3° in latitude. The changes of the shell with velocity are consistent with the picture of a large shell formed from the merger of several shells.

We find a kinematic distance to shell of 5.5 kpc, which implies a physical diameter of 490×290 pc. The velocity profile shows a clear bowl shape with increased brightness at the front and back caps. We therefore estimate an expansion velocity of 13 ± 6 km s^{-1}. We find an ambient density of $n_0 \approx 1.4$ cm^{-3} and a swept-up mass of 2.8×10^5 M$_\odot$. Given the radius, ambient density and expansion velocity we find that the expansion energy is 7×10^{51} ergs.

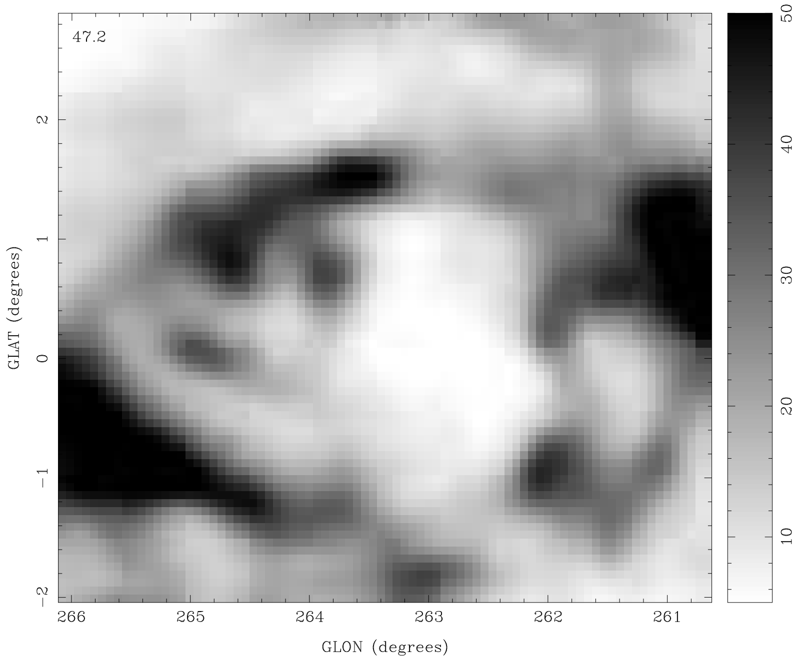

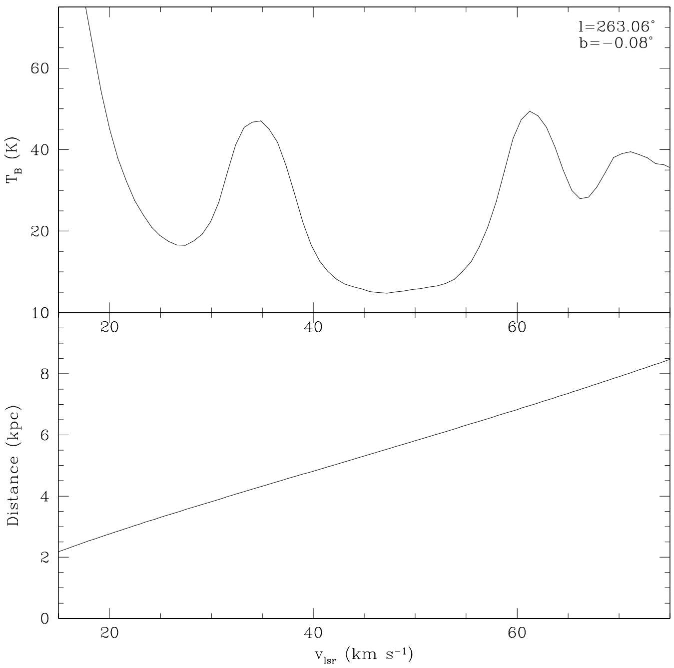

Figure 5.3: Grey-scale image of GSH 263+00+47 (top) and velocity profile through the shell, with the corresponding rotation curve along the line of sight (bottom). The grey-scale is linear in brightness temperature, as shown on the wedge at the right.

5.3.4 GSH 267-01+77

Like GSH 263+00+47, the morphology of GSH 270-01+77 is irregular. The shell, which is shown in Figure 5.4, changes shape dramatically with velocity, but maintains a very strongly emitting rim surrounding the H I void. It is likely that this, too, was formed by the merger of several spatially distinct shells. The velocity profile, though, is consistent throughout the shell and demonstrates clear edges. The expansion velocity is $v_{exp} = 18$ km s^{-1}. The kinematic distance is 9.2 kpc and the physical radii are 420×280 pc. We calculate an ambient density of $n_0 \approx 0.4$ cm^{-3} and a swept-up mass of 4.5×10^6 M$_\odot$. The large radius and expansion velocity lead to an expansion energy of 1.8×10^{53} ergs. It is perhaps more reasonable to consider the structure as three individual shells with radii on the order of 100 pc and expansion energies on the order of few $\times\, 10^{51}$ ergs. Because the expansion energy goes as $R_{sh}^{3.14}$, considering the system as three shells each of radius $R_{sh} = R_{\rm tot}/3$, the expansion energy for the system, $E_{\rm exp} = \sum_{i=1}^{3} E_i$, is decreased by a factor of ~ 10.

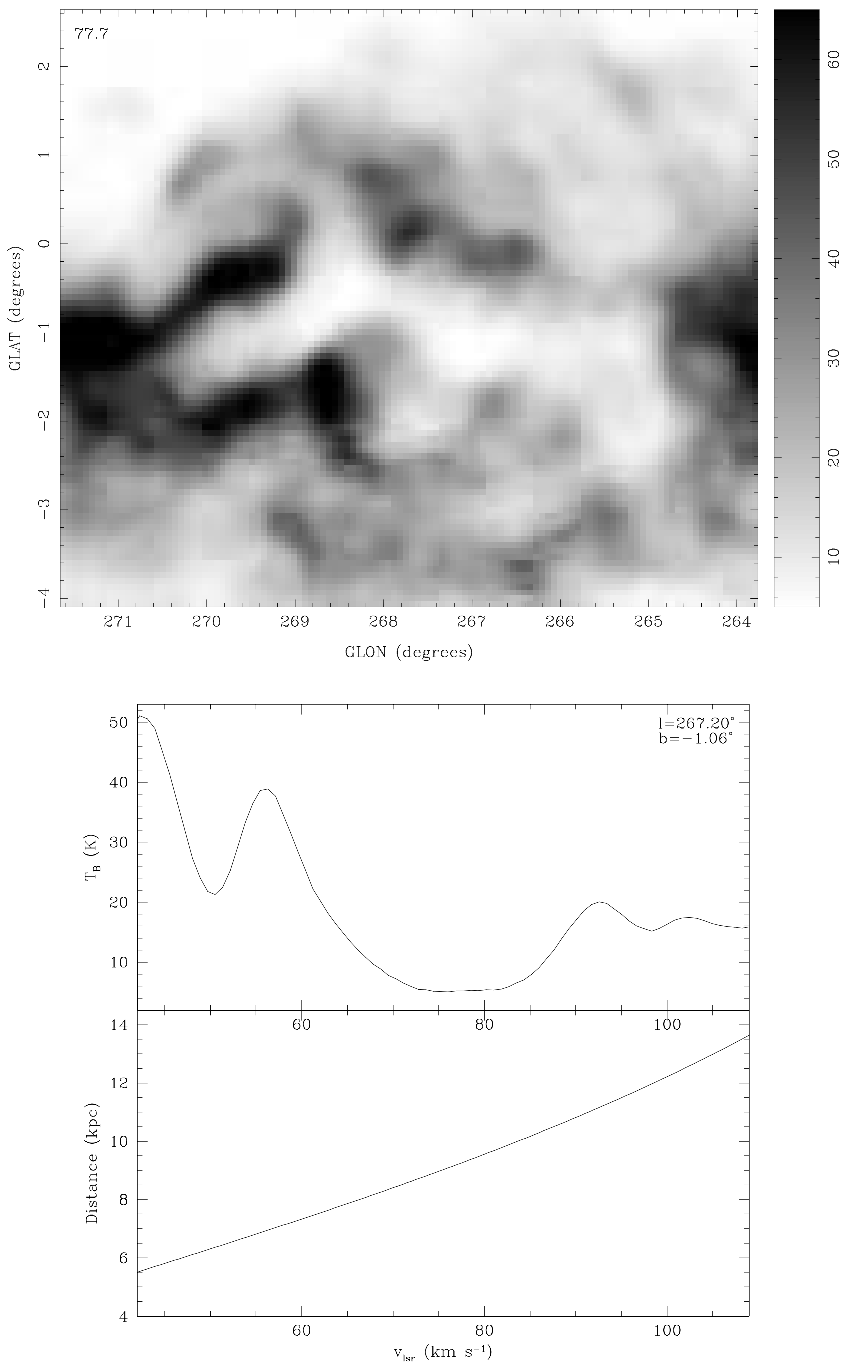

Figure 5.4: Grey-scale image of GSH 267-01+77 (top) and velocity profile through the shell, with the corresponding rotation curve along the line of sight (bottom). The grey-scale is linear in brightness temperature, as shown on the wedge at the right.

5.3.5 GSH 270-03+42

GSH 270-03+42 is about at 6 kpc distance in the region between the Sag-Carina and Perseus arms. As seen in Fig. 5.5, the shell has a very thin wall that extends around the entire circumference. This wall is a factor of $5-10$ brighter than the shell interior. There is also a faint ($T_b \sim 15$ K) filament at $b=-3^\circ$ that bisects the shell. At 6 kpc, the shell is 340×400 parsecs in diameter. We find an ambient density of $n_0 \approx 0.8$ cm^{-3} and a swept-up mass of 5.3×10^5 M$_\odot$. It has an expansion velocity of 12 km s^{-1} and an expansion energy of 1.1×10^{52} ergs.

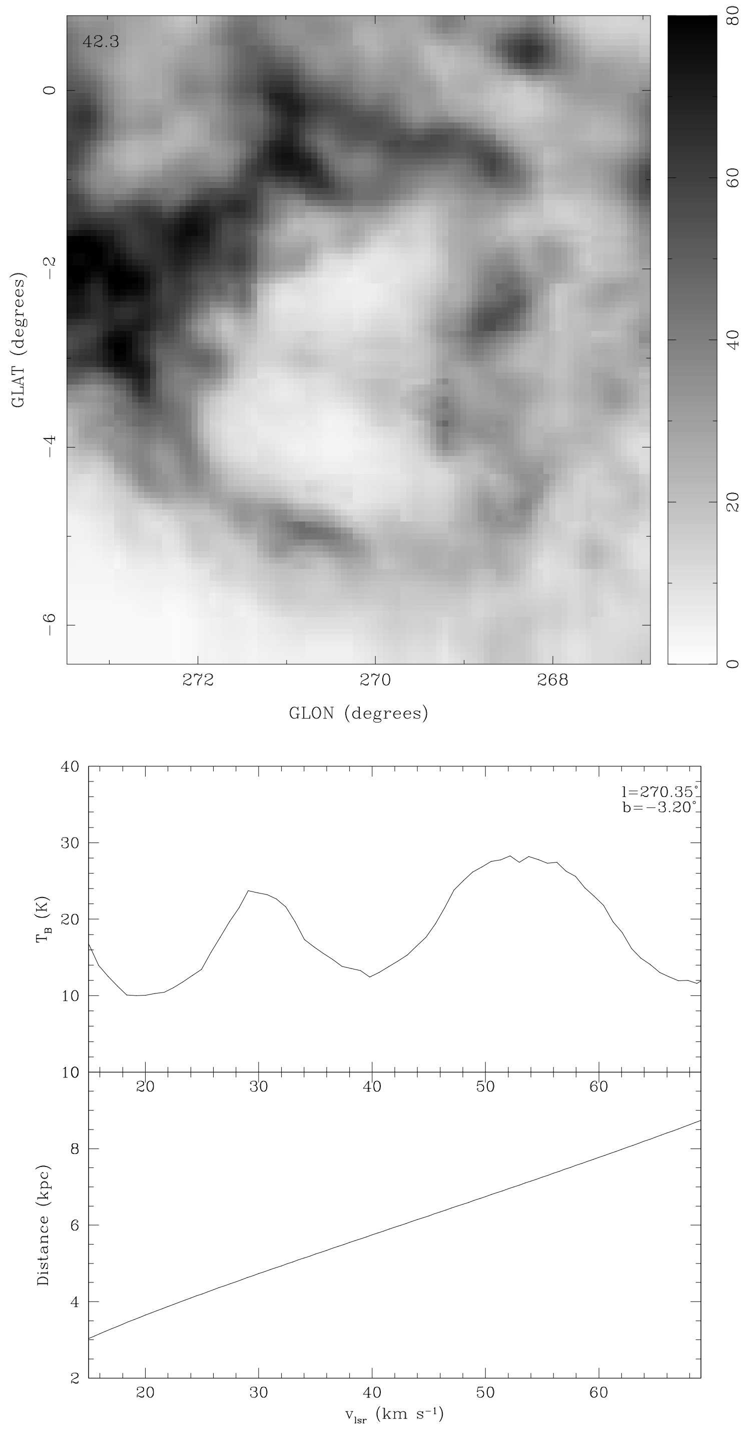

Figure 5.5: Grey-scale image of GSH 270-03+42 (top) and velocity profile through the shell, with the corresponding rotation curve along the line of sight (bottom). The grey-scale is linear as shown on the wedge at the right.

5.3.6 GSH 285-02+86

As seen in Figure 5.6, GSH 285-02+86 is a continuous shell with two H I filaments crossing the void near the center. Though it is possible that the shell is the interaction of three shells, the continuity of the outer rim, suggests that it is one structure. The velocity profile shows distinct near and far edges with a deep minimum at $v = 86$ km s^{-1}. The bad pixel seen in Fig. 5.6 is due to receiver saturation towards the bright H II region RCW 49. The kinematic distance for the shell based on the central velocity is 13.7 kpc. Both RCW 49 and the H II region, G287.39-00.63, on the top left edge of the shell, have recombination line radial velocities between ~ -15 and -24 km s^{-1}. These regions at distances between 3 and 4.9 kpc (Caswell & Haynes 1987), are much closer than the shell. These regions are coincident with the Car OB1 stellar association (Humphreys 1978). The radial velocity difference between the stellar association and the H I shell, however, eliminates this possibility despite the sky plane coincidence.

The velocity profile shows an expansion velocity of ~ 21 km s^{-1}. At this radius the shell has a radius of ~ 385 pc. We find an ambient density of $n_o \approx 0.5$ cm^{-3} and a swept-up mass of 4.4×10^6 M$_\odot$. We therefore calculate an expansion energy of 2.2×10^{53} ergs.

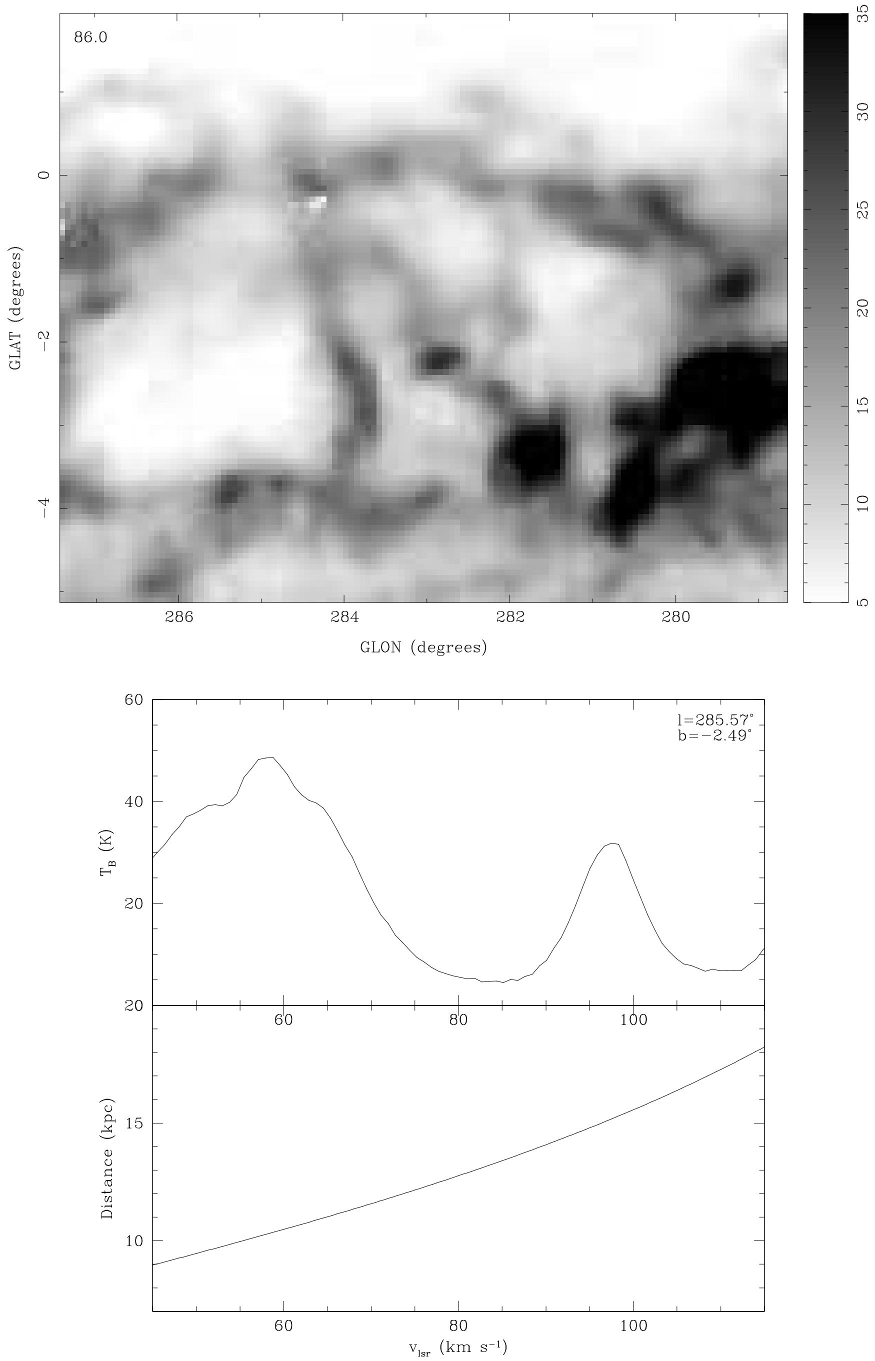

Figure 5.6: Grey-scale image of GSH 285-02+86 (top) and velocity profile through the shell, with the corresponding rotation curve along the line of sight (bottom). The grey-scale is linear in brightness temperature, as shown on the wedge at the right.

5.3.7 GSH 292-01+46

The Galactic plane near $l = 290°$ is particularly filled with holes. There are two large shells that nearly overlap in the plane of the sky, though in total they span more than 90 km s^{-1} in velocity space. GSH 292-01+46, the first of these two shells, is one of the clearest shells in the catalog. The walls are very distinct, as is the near cap at $v \sim +28$ km s^{-1}. The far side of the shell, near $v = +60$ km s^{-1}, clearly shows rings that decrease in size with increasing velocity. At the top edge of the shell there is an indentation in the wall that is flanked by two small clumps of gas that lie inside the main void. The nature of these is unclear. The velocity profile through the shell center shows over a factor of 15 increase in brightness temperature from the shell interior to the walls.

The expansion velocity is 21 km s^{-1}. The kinematic distance to the shell is 11.6 kpc and it has physical size of 515×200 pc. There is an H II region, G293.027–1.03, identified by recombination line emission (Caswell & Haynes 1987), located behind the shell. The position places the H II region against the far wall of the shell and it may therefore be associated with the shell, perhaps as a result of triggered star formation. The derived ambient density is $n_0 \approx 0.5$ cm^{-3} and the swept-up mass is 9.2×10^6 M$_\odot$. We estimate an expansion energy of 4.6×10^{53} ergs.

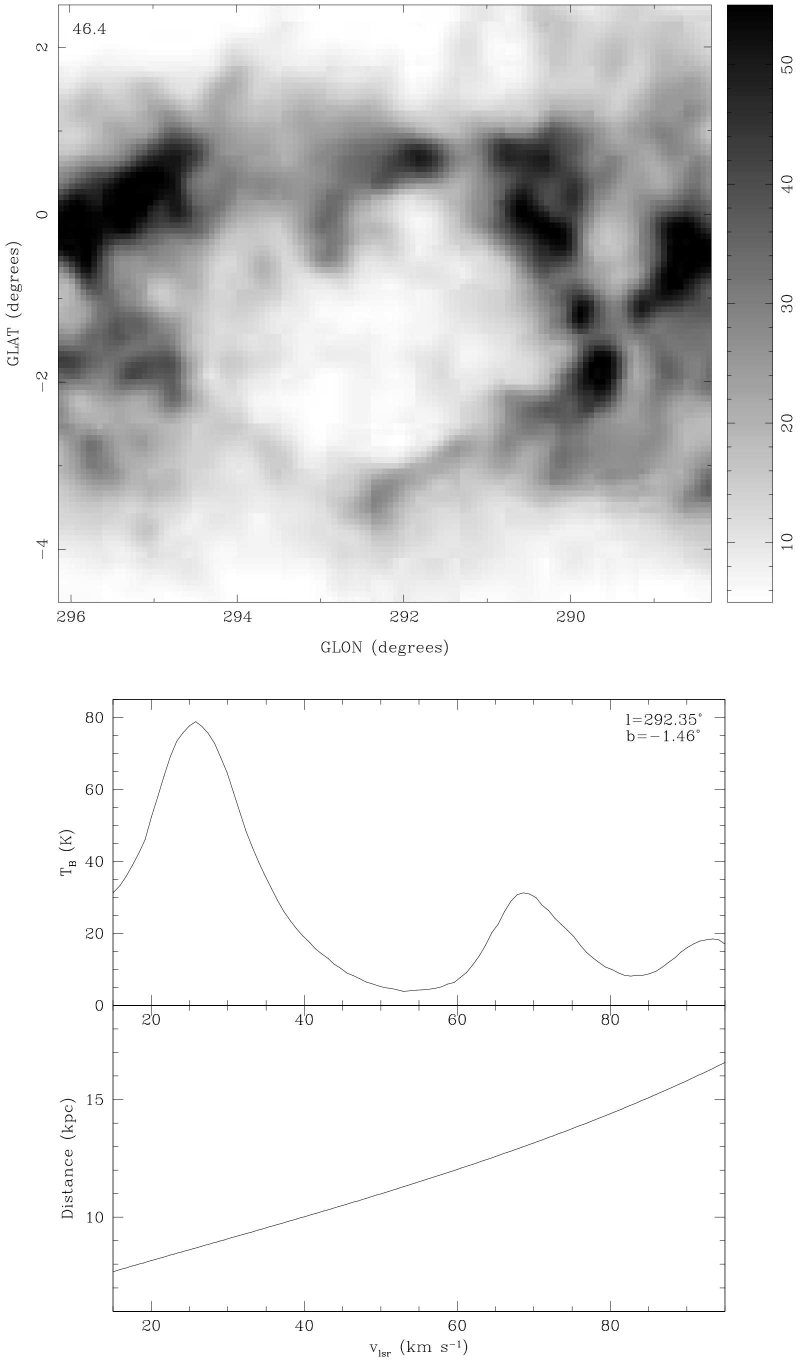

Figure 5.7: Grey-scale image of GSH 292-01+46 (top) and velocity profile through the shell, with the corresponding rotation curve along the line of sight (bottom). The grey-scale is linear in brightness temperature, as shown on the wedge at the right.

5.3.8 GSH 297-00+73

The large shell, GSH 297-00+73, is shown in Fig. 5.8. This shell appears to be a composite of two shells. There is a narrow wall separating the two original shells at $l = 297\overset{\circ}{.}2$. The wall is particularly strong near $v = 63$ km s^{-1} and $v = 92$ km s^{-1}. Near the center of the shell the wall disappears almost completely. The decrease in emission may be due to an increased level of ionization as a result of the collision of the two walls. The far-side caps of the left and right halves are observed at $v = 95$ km s^{-1} and $v = 100$ km s^{-1}, respectively. At these velocities the surrounding diffuse H I emission has dropped considerably and the caps of these shells are the brightest features by a factor of $\sim 2 - 3$. On the near side, both caps are visible at $v = 55$ km s^{-1}. The center velocity of $v = 73$ km s^{-1} gives a kinematic distance of 14.8 kpc. We calculated the column density through the center of one half and derived an ambient density of $n_0 \approx 0.3$ cm^{-3}, which may be an underestimate if we included too little of the caps in our column density calculation. However, using this number we find a swept-up mass of $\sim 1.4 \times 10^7$ M$_\odot$. If we interpret this shell as two, merged shells, one shell of $R_1 = 390$ pc, $v_{\rm exp1} = 23$ km s^{-1} and another of $R_2 = 315$ pc, $v_{\rm exp2} = 20$ km s^{-1}, then the total expansion energy is $E_E = E_1 + E_2 = 1.9 \times 10^{53}$ ergs. This shell is far away from any other evidence of star formation, there are no H II regions nearby nor any other tracers of spiral arms.

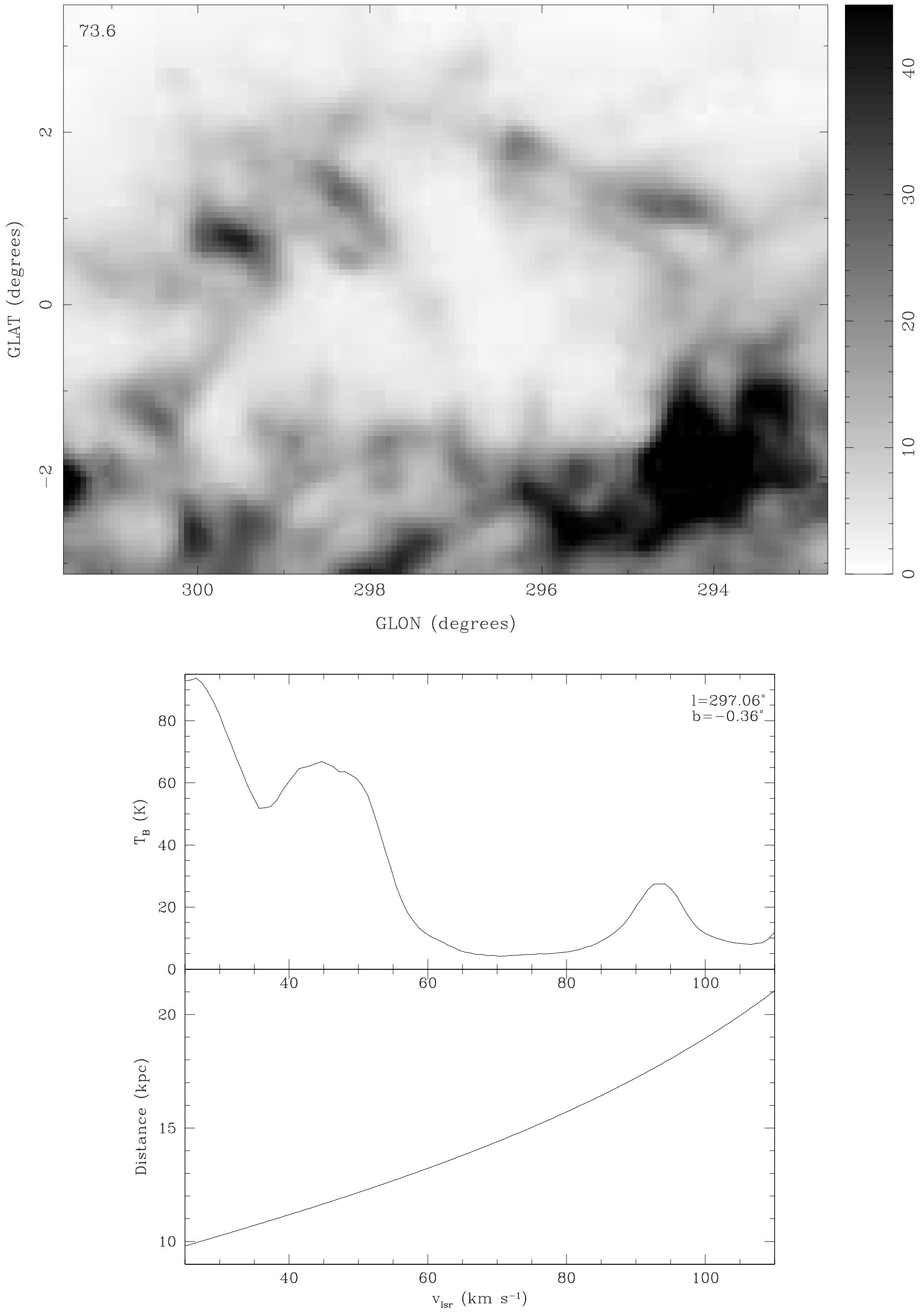

Figure 5.8: Grey-scale image of GSH 297-00+73 (top) and velocity profile through the shell, with the corresponding rotation curve along the line of sight (bottom). The grey-scale is linear in brightness temperature, as shown on the wedge at the right.

5.3.9 GSH 298-01+35

On the local side of GSH 297-00+73 is GSH 298-01+35. This unique structure, shown in Fig. 5.9, appears to be a chimney or "worm." It is very narrow in the longitudinal direction, but extends several degrees out of the plane. The chimney cuts through the Galactic plane at a slight angle and then opens above and below the plane. There is no evidence for closure within 6 degrees of the Galactic plane. At the center of the chimney is a spherical region of decreased emission that we believe is the shell origin at $l = 297\overset{\circ}{.}7$, $b = -0\overset{\circ}{.}7$. The velocity profile deviates dramatically from profiles on either side of the chimney. The large bowl, characteristic of shells, is only evident at the longitudes covering this chimney. The full-width of the bowl is 20 km s^{-1} implying an expansion velocity of $v_{exp} \sim 10$ km s^{-1}. The center velocity of the chimney is at $v = +35$ km s^{-1}, which gives the chimney a kinematic distance of 10.5 kpc, and places it near the edge of the Sagittarius-Carina spiral arm. At this distance the chimney is only 75 pc across but extends more than a kiloparsec above the plane. The conditions required to confine a shell so dramatically along the plane and still allow for expansion into the halo are unclear.

We derive an ambient density of ~ 4 cm^{-3} and assuming that the original cavity was spherical with a radius of ~ 75 pc, we find a swept-up mass of 4×10^5 M$_\odot$. We estimate the energy required to create the spherical cavity with the caveat that this may be a severe underestimate if the shell has been significantly confined along the plane. Assuming an expansion velocity of 10 km s^{-1}, we calculate an expansion energy of $\sim 1.1 \times 10^{52}$ ergs, which is comparable to the energy released by ten supernovae or through stellar winds over the course of the lifetime of ten stars. Near this position and velocity, between $v = +16$ km s^{-1} and $v = +31$ km s^{-1}, are several H II regions cataloged by Caswell & Haynes (1987). The closest H II region, G298.22-0.33, is at $v = +31$ km s^{-1} placing it near the center of the chimney.

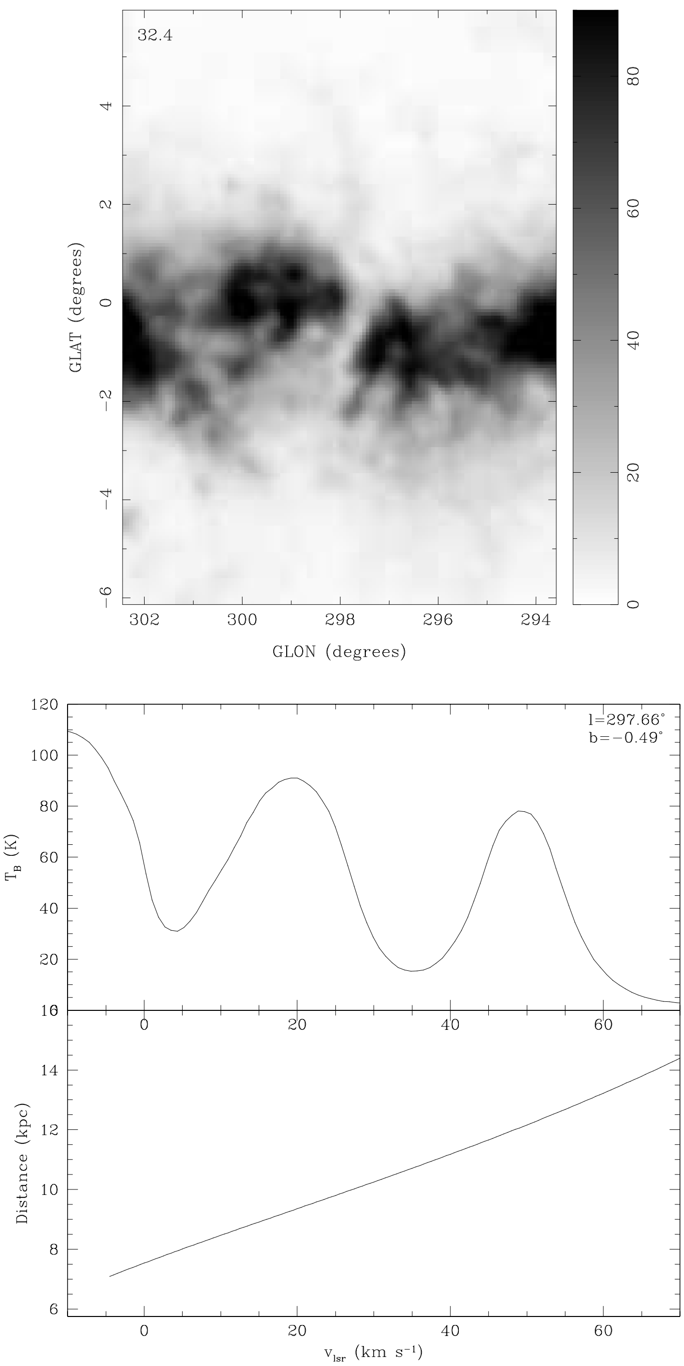

Figure 5.9: Grey-scale image of GSH 298-01+35 (top) and velocity profile through the shell, with the corresponding rotation curve along the line of sight (bottom). The grey-scale is linear in brightness temperature, as shown on the wedge at the right.

5.3.10 GSH 316-00+65

As seen in Figure 5.10, GSH 316-00+65 has two similarly sized halves. It is likely a composite of two shells. Both shells have nearly identical velocity profiles suggesting that they are adjacent at a distance 19.5 kpc. Because the two are joined at the same systemic velocity we define the entire structure as one shell. The component shells are $\sim 2^\circ$ in diameter, or ~ 680 pc each. The full shell has a physical size of about 700×600 pc. We find an expansion velocity of 16 km s^{-1} for the shell. We calculate an ambient density of $n_0 \approx 0.1$ cm^{-3}, which seems surprisingly low, however, given the extreme distance of the shell it may be representative of its position. Using this ambient density we calculate a swept-up mass of 6.9×10^6 M$_\odot$. We calculate the expansion energy required to form the individual shells and take the sum to be the expansion energy of the composite shell. Therefore, we find a total expansion energy of 1.5×10^{52} ergs. Despite the large size of these shells, the composite energy is quite low as a result of the very low ambient density.

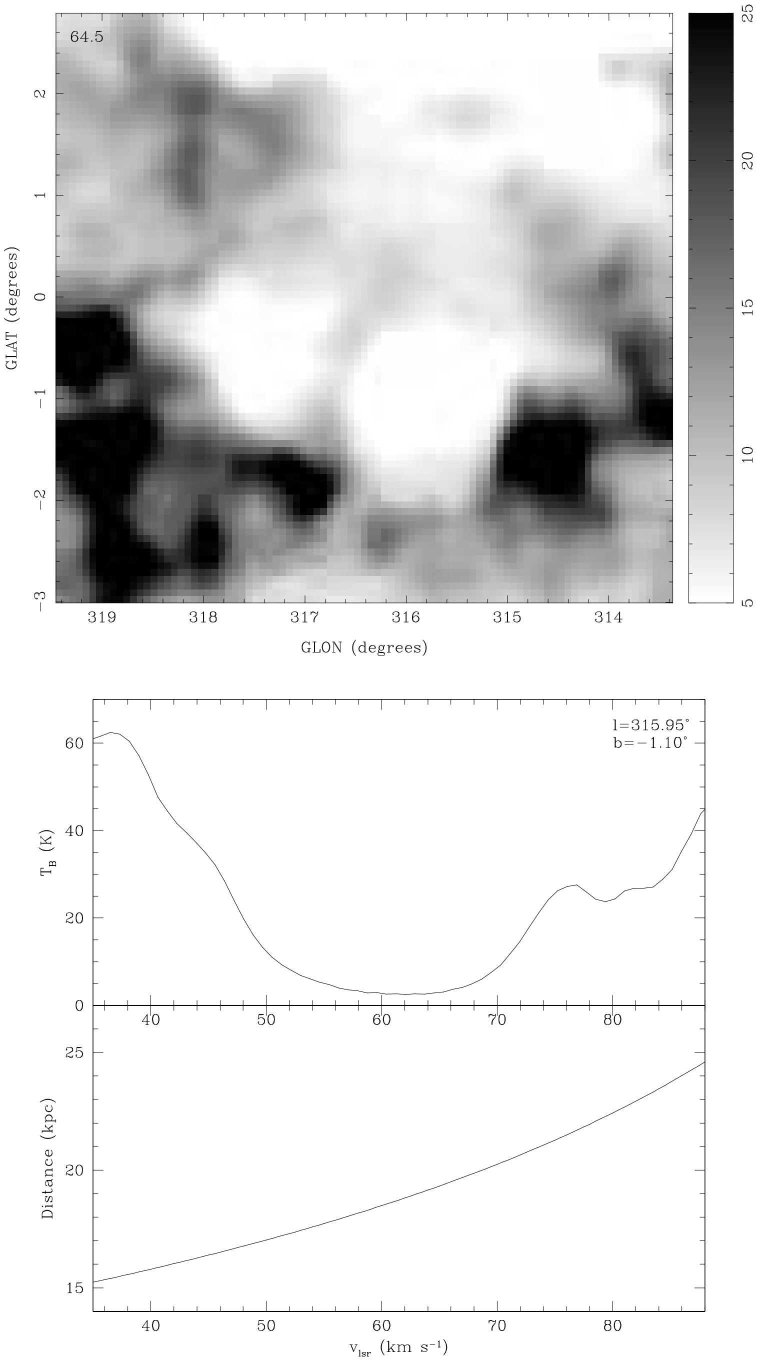

Figure 5.10: Grey-scale image of GSH 316-00+65 (top) and velocity profile through the shell, with the corresponding rotation curve along the line of sight (bottom). The grey-scale is linear in brightness temperature, as shown on the wedge at the right.

5.3.11 GSH 319-01+14

GSH 319-01+14 is shown in Figure 5.11. This shell is small in angular diameter, spanning only 2°. However, the shell is very dramatic with a density contrast of ~ 11 between the center and the edges. The brightness temperature in the center is as low as ~ 4 K. The far cap is clearly detected at $v = 36$ km s^{-1}. The near cap, however, is more difficult to detect because of confusion with local gas near $v = 3$ km s^{-1}. The kinematic distance, based on a central velocity of $v = 14$ km s^{-1}, is 14.0 ± 0.9 kpc. Assuming this distance the shell has a physical diameter of 520×412 pc. We calculate an ambient density of $n_0 \approx 0.5$ cm^{-3} and a swept-up mass of 1.3×10^6 M$_\odot$. The expansion velocity is ~ 18 km s^{-1} and the energy $E_E \approx 4.8 \times 10^{52}$ ergs.

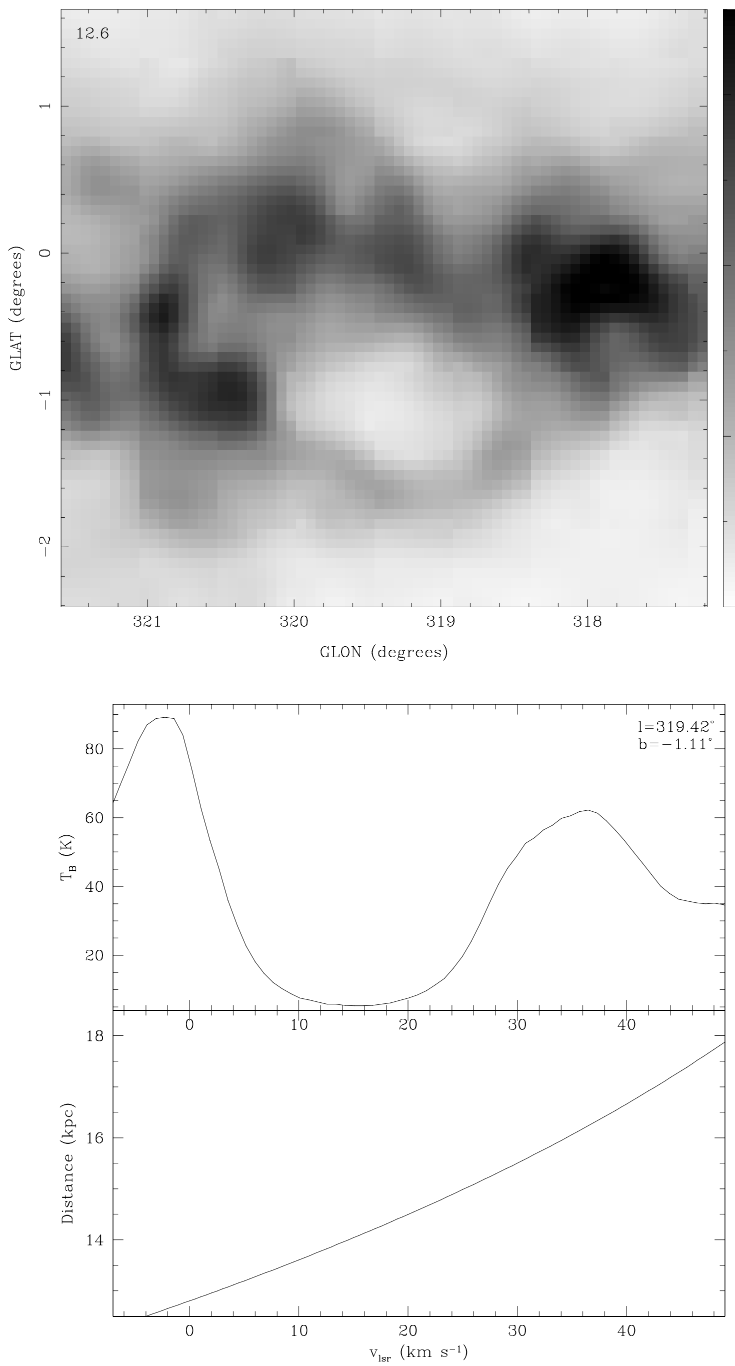

Figure 5.11: Grey-scale image of GSH 319-01+14 (top) and velocity profile through the shell, with the corresponding rotation curve along the line of sight (bottom). The grey-scale is linear in brightness temperature, as shown on the wedge at the right.

5.3.12 GSH 327+04-25

As discussed above, shells in the inner Galaxy are considerably more difficult to detect because of confusion with emission from gas at two distances. However, as seen in Figure 5.12, GSH 327+04-25 is quite distinct. This shell is situated slightly above the Galactic plane and the ellipse of emission is oriented at $\sim -15°$ with respect to the plane. This is the only non-composite shell in the catalog with a significantly skewed orientation with respect to the plane. Kinematic distances place the shell at either 1.9 or 12.4 kpc. Its large angular diameter suggests that it is at the near distance with a physical size of 260×180 pc. At the far distance this shell would have a diameter on the order of 1.5 kpc. We detect shells at both of these sizes and distances and it is therefore difficult to determine the true distance. Because smaller shells require less energetic creation events we prefer to assume that this shell is at the near distance. We note, though, that this determination is tentative and all derived parameters should also be considered tentative.

The shell has an apparent expansion velocity of 7 km s^{-1}. However, the inner Galaxy emission has a large filling factor that makes it difficult to determine expansion velocities with great certainty. In addition, it is not possible to calculate an ambient density using the method described above so, as with the other inner Galaxy shells, we assume $n_0 = 1$ cm^{-3}. We therefore calculate a swept-up mass of 2.2×10^5 M$_\odot$ and an expansion energy of 3×10^{51} ergs.

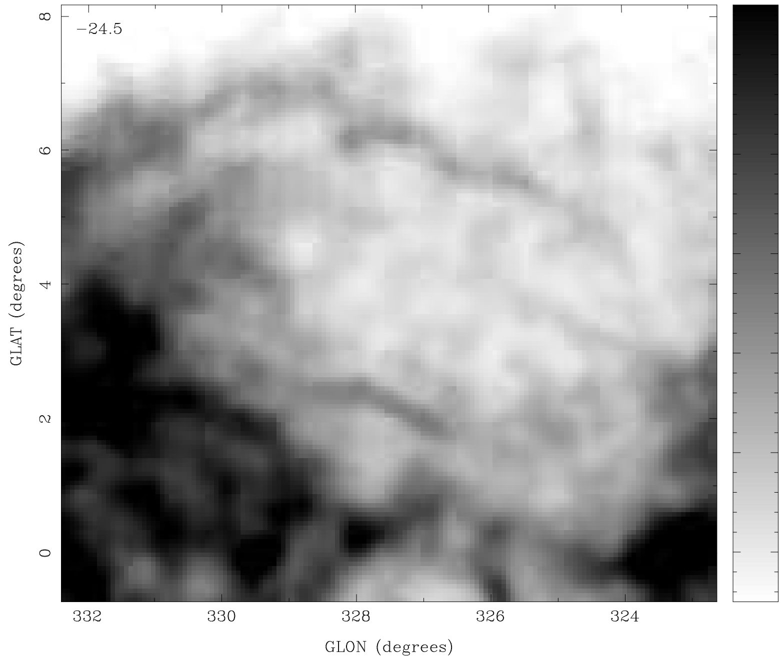

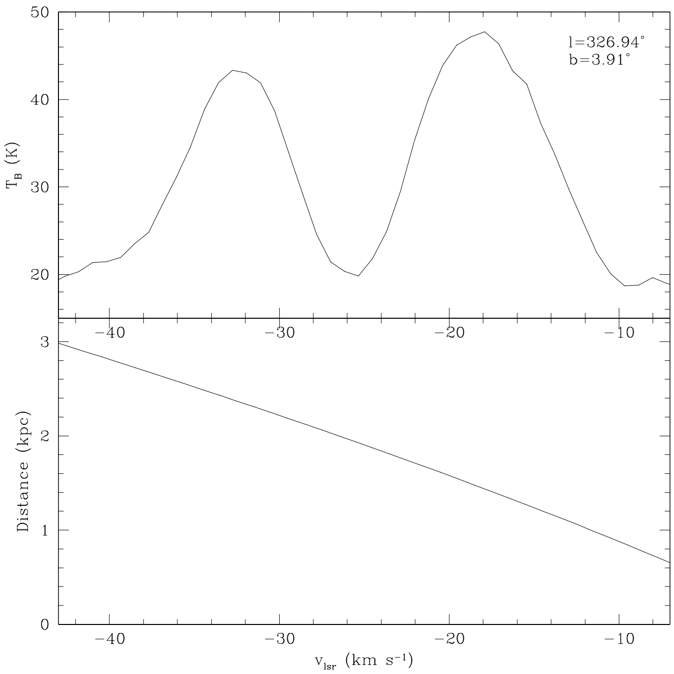

Figure 5.12: Grey-scale image of GSH 327+04-25 (top) and velocity profile through the shell, with the corresponding rotation curve along the line of sight (bottom). The grey-scale is linear in brightness temperature, as shown on the wedge at the right.

5.3.13 GSH 337+00–05

Figure 5.13 is an image of a large angular diameter shell, GSH 337+00–05. GSH 337+00–05 is reminiscent of the Coalsack shell, GSH 304-00-12, discussed in Chapter 4. The shell has a very thin rim and a very regular elliptical shape. The H I void is bisected by emission from the Galactic Plane. Kinematic distances for the shell are 570 pc or 15 kpc. The very low velocity, however, makes these distances quite uncertain. At the near distance the shell has a size of 185×125 pc, whereas at the far distance it would have a diameter of nearly 4 kpc. We find the latter possibility unlikely and therefore place the shell at ~ 570 pc, on the near edge of the Sagittarius-Carina arm. Again, with some uncertainty we find an expansion velocity of 9 km s^{-1}. We assume an ambient density of 1 cm^{-3} and calculate a swept-up mass of 1×10^5 M$_\odot$. From the radius and expansion velocity we calculate an expansion energy of 1.6×10^{51} ergs.

The shell may be correlated with Ara OB1a, an association of 14 O, B, and A stars at an adopted distance of 1.38 kpc. The stars are distributed between $l = 335°$ to $l = 341°$ and $b = \pm 3°$, which places them in the boundaries of shell. Distance moduli for the individual stars indicate distances between 790 and 2125 pc, with a mean distance of 1460 ± 125. Additionally, stars with measured radial velocities are between -20 km s^{-1} and $+5$ km s^{-1}, which agrees well with the central velocity of the shell. These coincidences seem to suggest that the cluster and shell are related. If we assume that the association has 14 stars each with a representative stellar wind luminosity of $L_w \sim 6 \times 10^{35}$ ergs s^{-1}, corresponding to that of a B0 star, we find that the expansion energy of the shell is consistent with formation by this cluster with an age of ~ 6 Myr. Because of large uncertainties in the distance of the H I shell ($D = 0.6 \pm 0.9$) a definitive identification is not possible.

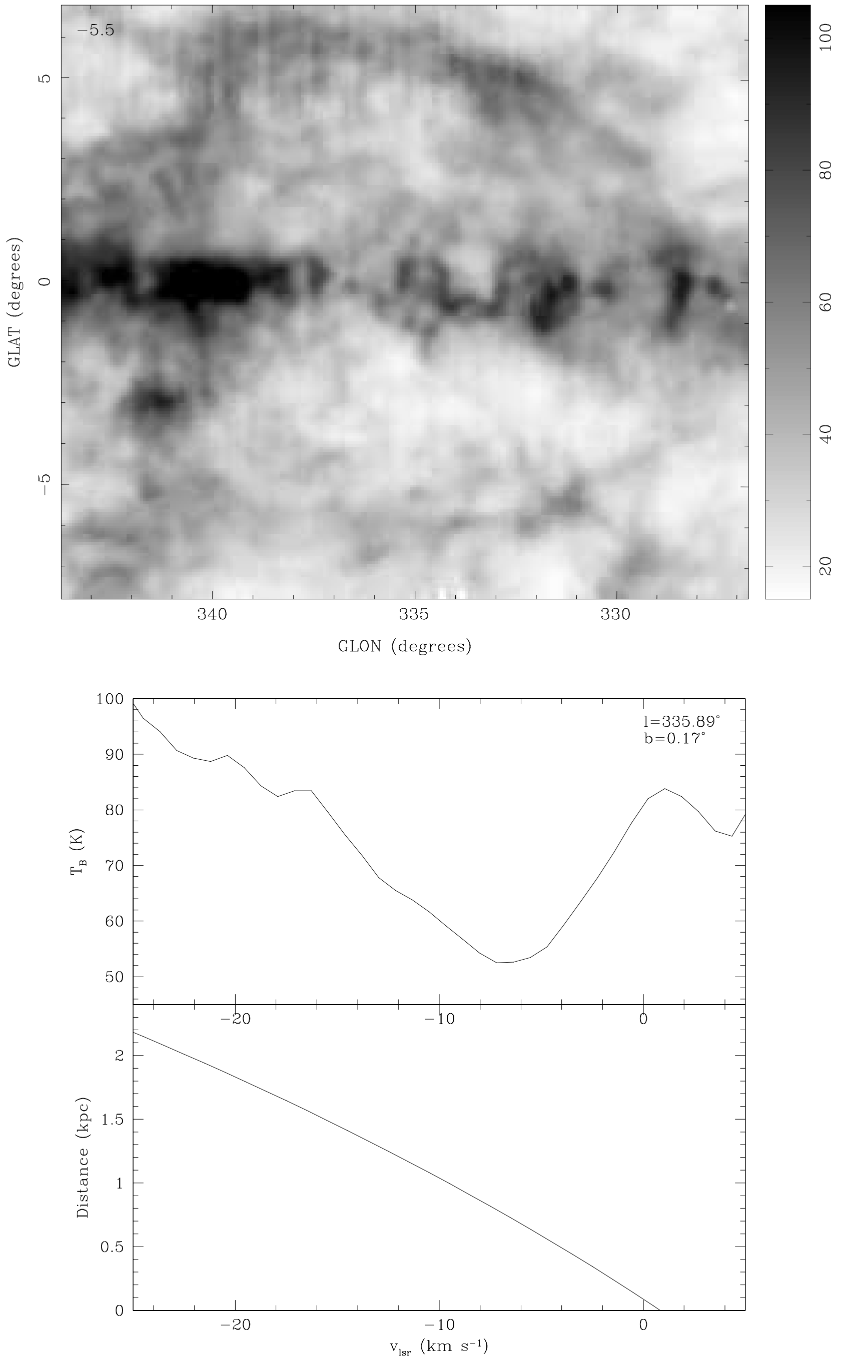

Figure 5.13: Grey-scale image of GSH 337+00–05 (top) and velocity profile through the shell, with the corresponding rotation curve along the line of sight (bottom). The grey-scale is linear in brightness temperature, as shown on the wedge at the right.

5.3.14 GSH 342–02–27

GSH 342–02–27 is a very small angular diameter shell shown in Figure 5.14. The shell has a clear velocity profile delineating both the near and far caps, as well as a fully intact rim. The kinematic distances are 2.6 or 13.5 kpc. In this case, the small angular diameter does not preclude either distance. At the near distance the shell has a diameter of 85 pc, and at the far distance it has a diameter of 442 pc. Assuming the a near distance the swept-up mass is 1×10^4 $M_\odot$ whereas at a distance of 13.5 kpc, the swept-up mass is 1.5×10^6 $M_\odot$. The expansion velocity is 14 km s^{-1}. We calculate an expansion energy of 2.5×10^{50} ergs for a radius of 42 pc and a tentative energy of 4.5×10^{52} ergs for a radius of 221 pc.

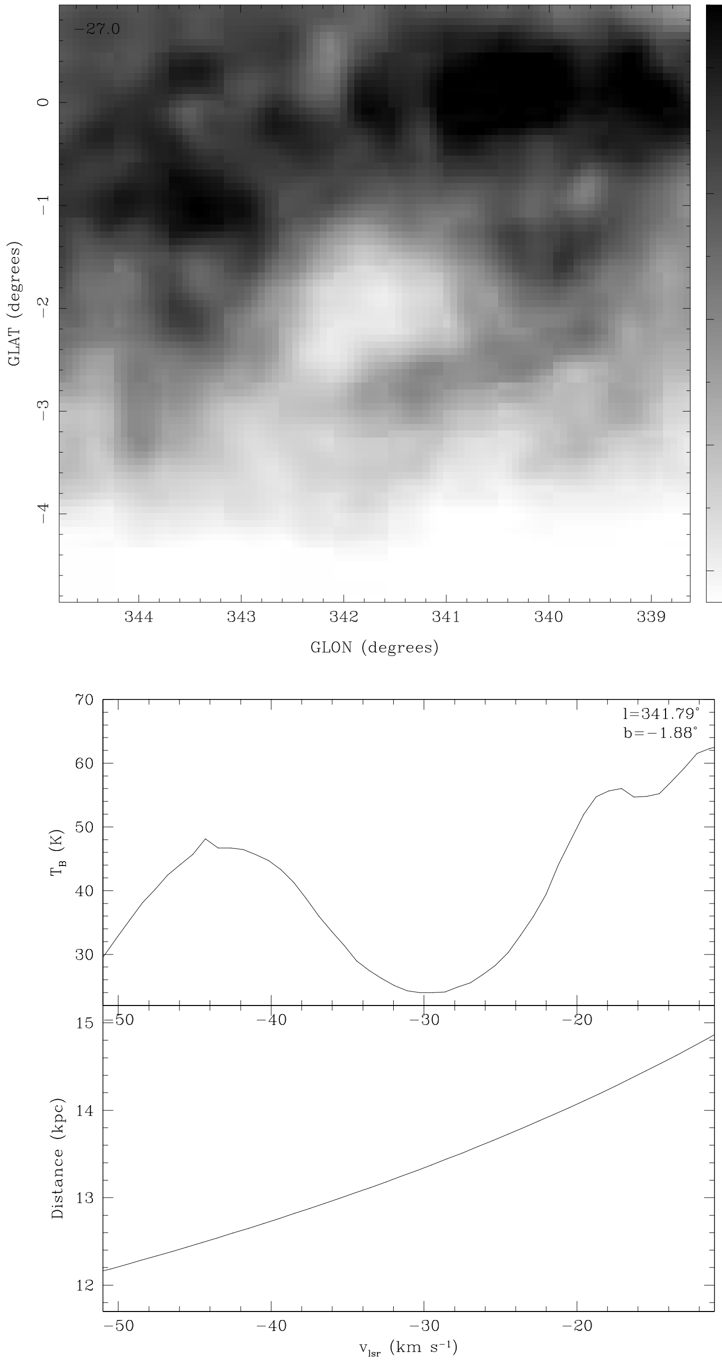

Figure 5.14: Grey-scale image of GSH 342–02–27 (top) and velocity profile through the shell, with the corresponding rotation curve along the line of sight (bottom). The grey-scale is linear as shown on the wedge at the right.

5.3.15 GSH 345+00+30

GSH 345+00+30 is a poorly defined shell at a large positive velocity (see Figure 5.15). The kinematic distance is 25.8 kpc, placing the shell on the far-side of the Galaxy. This distance leads to a physical radius on the order of 2 kpc. However, velocity crowding becomes significant at high longitudes (i.e $l \gtrsim 345°$) making distance determinations increasingly more difficult. Furthermore gas near the Galactic center experiences extreme non-circular motions on the order of 20-30 km s^{-1} (Burton 1988). We believe, then, that the distance for this shell is too poorly defined to attempt analysis of its distance dependent properties.

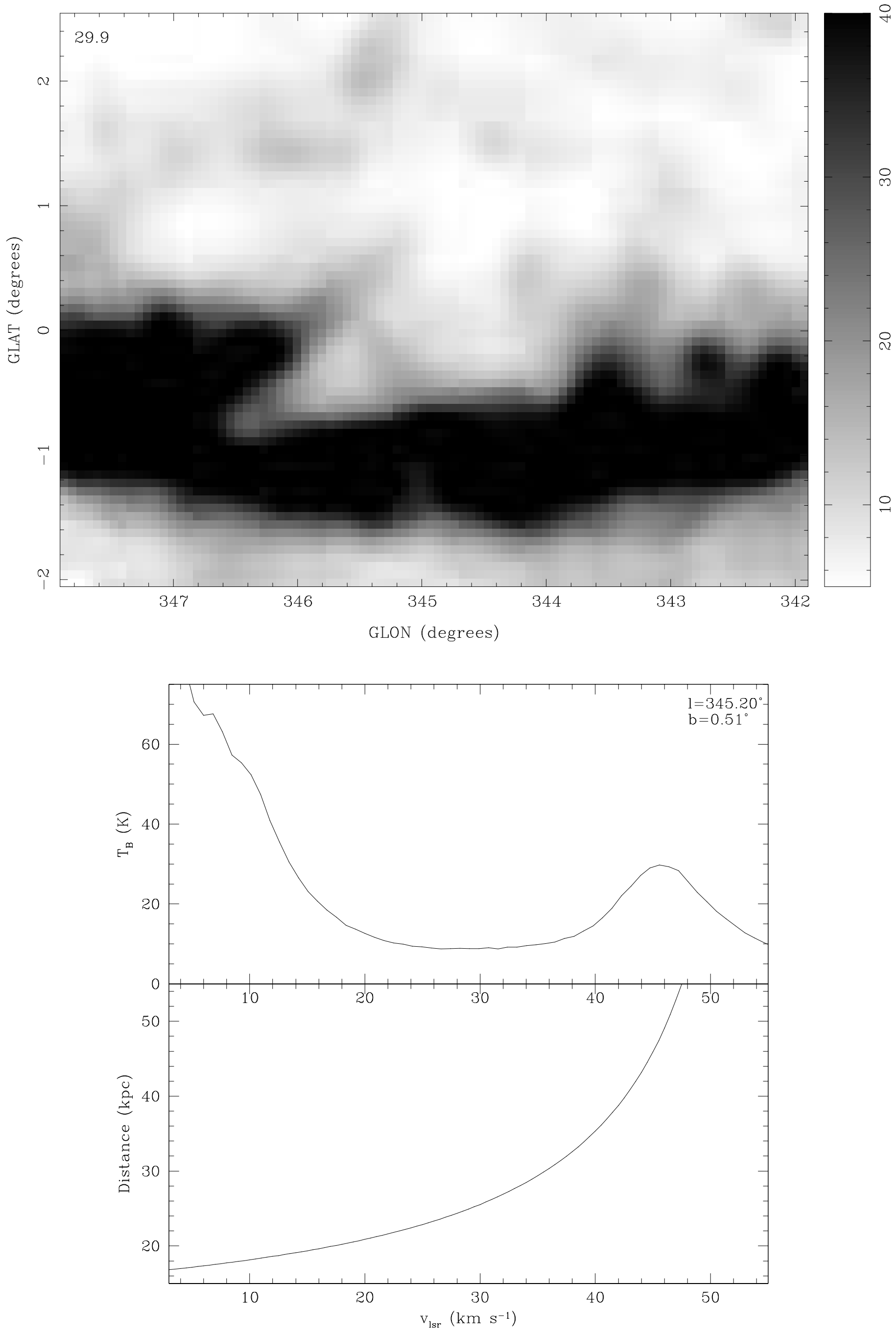

Figure 5.15: Grey-scale image of GSH 345+00+30 (top) and velocity profile through the shell, with the corresponding rotation curve along the line of sight (bottom). The grey-scale is linear in brightness temperature, as shown on the wedge at the right.

Table 5.1: New H I shells from the SGPS

Name	l (deg)	b (deg)	v^a (km s^{-1})	Δl (deg)	Δb (deg)	$v_{\rm exp}$ (km s^{-1})	Comments
GSH $255-00+52$	255.2	-0.5	$+52$	3.8	3.7	18	
GSH $256+00+63$	256.6	-0.1	$+63$	2.2	2.2	12	
GSH $263+00+47$	262.9	-0.1	$+47$	2.3	2.9	13	irregular shape
GSH $267-01+77$	267.1	-1.1	$+77$	5.3	3.5	18	two merged shells
GSH $270-03+42$	270.5	-3.3	$+42$	3.2	3.8	12	
GSH $277+00+36^b$	277.5	0.0	$+36$	5.4	>20	20	proposed chimney
GSH $280+00+59^{\rm b}$	279.8	$+0.1$	$+59$	2.6	>20	15	proposed chimney
GSH $285-02+86$	285.6	-2.5	$+86$	3.3	3.2	21	
GSH $292-01+55$	292.4	-1.5	$+55$	5.1	2.0	21	
GSH $297-00+73$	297.2	-0.3	$+73$	5.5	2.8	21	two merged shells
GSH $298-01+35$	297.7	-0.5	$+35$	0.8	>12	10	proposed chimney
GSH $304-00-12^c$	303.9	-0.2	-12	29	20	9	Coalsack shell
GSH $305+01-24^c$	305.1	$+1.0$	-24	7	11.3	6	assoc. w/ Cen OB1
GSH $316-00+65$	316.4	-0.5	$+65$	4.1	3.0	16	two merged shells
GSH $319-01+13$	319.4	-1.1	$+13$	2.1	1.7	18	
GSH $327+04-25$	327.2	$+3.4$	-25	7.7	5.6	7	
GSH $337+00-05$	335.9	$+0.2$	-5	18.6	12.5	9	assoc. w/Ara OB1a
GSH $342-02-27$	341.8	-1.9	-27	1.8	1.9	14	
GSH $345+00+30$	345.2	$+0.5$	$+30$	4.7	2.5	18	unknown distance

[a]All velocities all quoted with respect to the local standard of rest (LSR).

[b]From McClure-Griffiths et al. (2000).

[c]From McClure-Griffiths et al. (2001a).

5.4 General Shell Properties

The SGPS shell catalog is, at this time, too small to perform a complete statistical analysis. The inclusion of the northern Heiles (1979, 1984) catalogs significantly increases the sample numbers. Heiles (1984) notes, though, that his catalog is unsuitable for statistics because of the subjective nature of identifying shells. The criteria he employs are less stringent than those employed here, so the catalogs are not well-matched. In the Heiles (1979, 1984) catalogs some shells are identified based on a single, arched filament at one velocity, velocity profiles are not available to be used as a selection criterion, and there is a selection effect against small angular diameter shells. However, we believe there is some value in examining the size, expansion velocity and energy distributions of all the cataloged shells and comparing those to other galaxies. Shells that have been

Table 5.2: Derived properties for new H I shells from the SGPS

Name	D (kpc)	R_{gal} (kpc)	$R_{\rm major}$ (pc)	$R_{\rm minor}$ (pc)	t_D (Myr)	n_0 (cm^{-3})	M (10^5 $M_\odot$)	E_E (10^{51} ergs)
GSH 255 − 00 + 52	5.3 ± 1.0	11.1 ± 0.7	175 ± 30	170 ± 30	5.7	1.7 ± 0.5	13 ± 7	53 ± 39
GSH 256 + 00 + 63	6.5 ± 1.0	11.9 ± 0.8	145 ± 20	140 ± 20	7.1	1.0 ± 0.4	4.2 ± 1.9	9 ± 7
GSH 263 + 00 + 47	5.5 ± 1.0	10.7 ± 0.6	110 ± 20	140 ± 25	5.0	1.4 ± 0.6	2.8 ± 1.5	7 ± 5
GSH 267 − 01 + 77	9.2 ± 1.2	12.9 ± 0.9	420 ± 55	280 ± 35	13.8	0.4 ± 0.1	45 ± 17	177 ± 104
GSH 270 − 03 + 42	6.0 ± 1.0	10.4 ± 0.6	170 ± 30	200 ± 30	8.4	0.8 ± 0.2	5.3 ± 2.6	11 ± 8
GSH 277 + 00 + 36	6.5 ± 0.9	10.0 ± 0.5	305 ± 45	> 1000	9.0	1.2 ± 0.1	27-56	240 ± 120
GSH 280 + 00 + 59	9.4 ± 0.9	11.5 ± 0.7	215 ± 20	> 1000	8.5	0.6 ± 0.1	11 ± 2	26 ± 10
GSH 285 − 02 + 86	13.7 ± 1.3	14.0 ± 1.0	395 ± 40	375 ± 35	11.1	0.5 ± 0.1	44 ± 13	218 ± 93
GSH 292 − 01 + 55	11.6 ± 1.0	11.5 ± 0.8	515 ± 45	200 ± 20	14.5	0.5 ± 0.1	92 ± 24	464 ± 196
GSH 297 − 00 + 73	14.7 ± 1.0	13.3 ± 1.0	710 ± 50	360 ± 25	20.0	0.3 ± 0.1	140 ± 29	190 ± 67
GSH 298 − 01 + 35	10.9 ± 0.9	10.2 ± 0.7	75 ± 6	> 1200	4.4	4.1 ± 1.3	2.3 ± 0.6	11 ± 5
GSH 304 − 00 − 12	1.2 ± 0.6 [a]	7.9 ± 0.4	280 ± 140	200 ± 100	18.4	...	19 ± 8	31 ± 28
GSH 305 + 01 − 24	2.2 ± 0.6	7.4 ± 0.3	140 ± 40	220 ± 60	13.8	...	3.9 ± 1.1	8.3 ± 7.1
GSH 316 − 00 + 65	19.5 ± 1.8	14.5 ± 1.5	700 ± 65	500 ± 45	25.9	0.1 ± 0.1	69 ± 19	15 ± 7
GSH 319 − 01 + 13	14.0 ± 0.9	9.3 ± 0.7	260 ± 15	200 ± 15	12.8	0.5 ± 0.1	13 ± 3	48 ± 14
GSH 327 + 04 − 25	1.9 ± 0.6	7.0 ± 0.5	130 ± 40	90 ± 30	11.0	...	2.2 ± 0.7	3 ± 3
GSH 337 + 00 − 05	0.6 ± 0.9	7.9 ± 0.7	90 ± 150	60 ± 100	5.9	...	1.0 ± 1.7	1.6 ± 7
GSH 342 − 02 − 27	2.6 ± 0.7 [b]	6.1 ± 0.6	40 ± 10	40 ± 10	1.7	...	0.1 ± 0.09	0.25 ± 0.23
GSH 345 + 00 + 30	25.8 ± 6.6 [c]	17.5 ± 4.6	...	...	...	...	...	

[a]For dual-valued distances the distance determination, where possible, is discussed in the text.

[b]It was not possible to resolve the distance ambiguity for this shell so parameters are calculated for both distances in the text. In the interest of space, only parameters calculated for the near distance are given in the table.

[c]Distance unknown

improperly cataloged may stand-out from the typical distributions. In addition, the differences from other galaxies may highlight other biases in Milky Way surveys.

Plotted in Fig. 5.16 are H I shell expansion velocities versus radius for the SGPS and Heiles (1979) shells. SGPS shells are plotted as asterisks and the Heiles shells are marked with triangles. Lines of constant dynamic age, as defined by equation 5.3, are marked with dashed lines. We find that most shells have dynamic ages between 5 and 15 Myr and all but two are younger than 25 Myr, which is consistent with the timescales for shell destruction by shearing and turbulent motions (Tenorio-Tagle & Bodenheimer 1988). The two shells with larger ages may be skewed by their extremely large radii. Also marked on the plot with dotted lines are contours of constant expansion energy, E_{51}, in units of 10^{51} ergs, as defined above. The one SGPS shell that lies above the $E_{51} = 1000$ line is GSH 316–00+65 which, as explained above, likely has an anomalous expansion energy because it is the merger of two shells. Shells with energies below $E_E \approx 1 \times 10^{51}$ ergs are selected against in this survey because of the large angular resolution and requirement that expansion be detected.

Figure 5.17 is a histogram of all shell radii from the Heiles and SGPS catalogs. Following the study of Oey & Clarke (1997) on the distribution of superbubble sizes in galaxies, we have binned these data logarithmically. As found to be the case with Holmberg II, M31, M33, and the SMC in Oey & Clarke (1997), the Galaxy exhibits a peak in the distribution near a few hundred parsecs and then a power-law decrease with shell size. The peak of the Milky Way distribution at $R \approx 225$ pc is larger than that observed in the SMC, M31 and M33. The peak is comparable to that of Holmberg II, which as a Magellanic irregular galaxy, undoubtedly experiences different effects from the Milky Way. The difference from M31 and M33, both disk galaxies, is more surprising, but we attribute this to the incompleteness of our current sample. The sample numbers limit our ability to estimate parameters related to the distribution. In particular, the last three bins at $\log R = 3.05$, 3.15, and 3.25 are of questionable

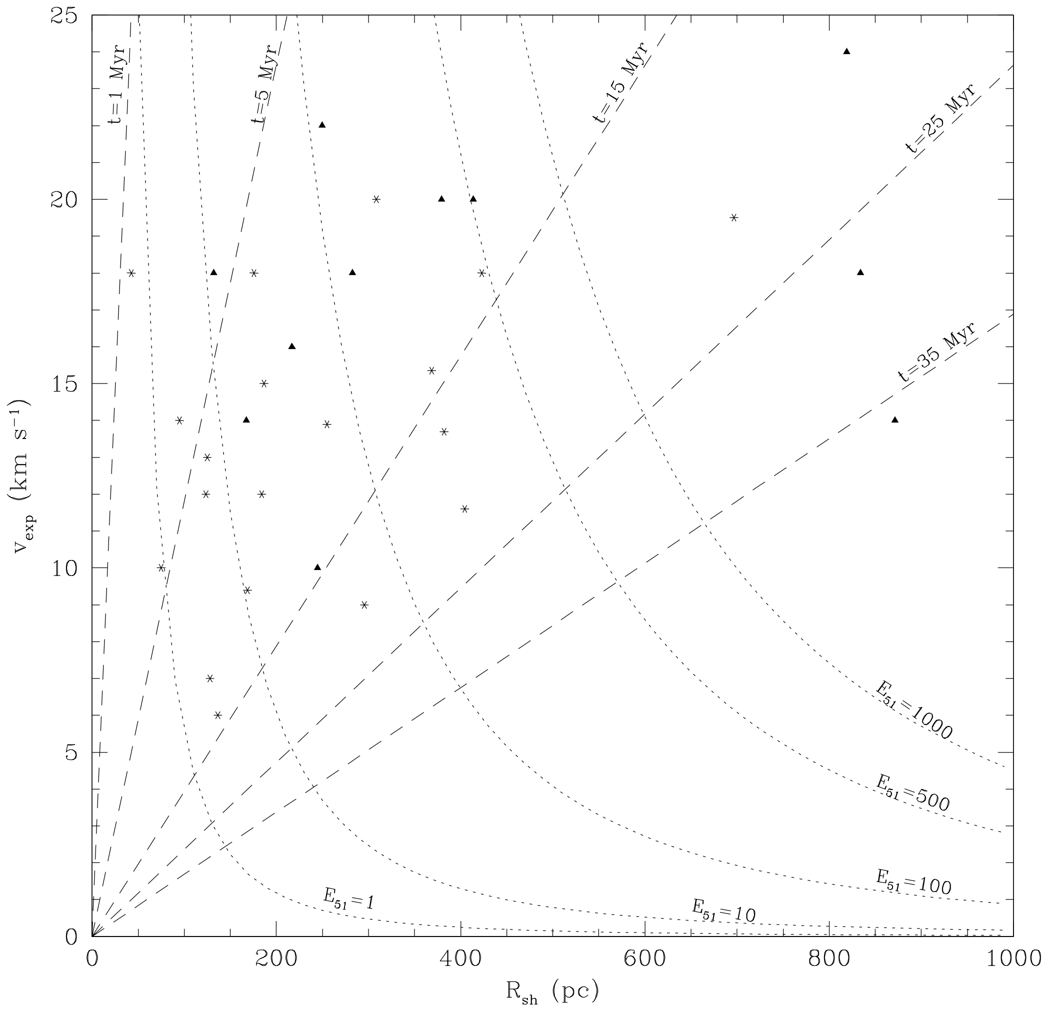

Figure 5.16: Expansion velocities of H I shells versus radius. Asterisks mark SGPS shells and triangles mark expanding shells from Heiles (1979). The dashed lines mark dynamic age estimates in mega-years and the dotted lines mark total expansion energy as defined by Chevalier (1974). Expansion energies are given in units of 10^{51} ergs.

statistical significance, each bin containing only a few shells.

Oey & Clarke (1997) show that radius distributions are well-fit by a power-law function, $N(R) \propto R^{-\alpha_r}$. The logarithmically binned data are fit linearly by $N(R) = \gamma_r R + \delta_r$, where $\gamma_r = 1 - \alpha_r$. This power-law distribution is an expected outcome for a population of shells formed from OB associations in a uniform ISM with a simple creation rate and mechanical luminosity function. Each of the galaxies examined by Oey & Clarke (1997) is fit with this power-law between the distribution peak and the cut-off radius, beyond which shells are not observed. In the case of the SMC, M31, and M33 the cut-off radius is around 400 pc (Stanimirović et al. 1999); Holmberg II has a cut-off at 800 pc. Included on Fig. 5.17 are two power-law fits to our data. The dotted line is a fit to a cut-off radius of 900 pc, which excludes the last three bins with large errors. This fit gives $\alpha_r = 1.6 \pm 0.2$. If we include the last three bins we find a cut-off radius of 1400 pc and $\alpha_r = 1.9 \pm 0.2$. This fit is shown on Fig. 5.17 with a dashed line. These power indices are slightly smaller than those found for external galaxies. Stanimirović et al. (1999) notes, however, that the average index is $\langle \alpha_r \rangle = 2.2 \pm 0.4$, which agrees within the errors with our fit to a cut-off radius of 1400 pc.

It has been suggested that the cut-off radius may correspond to the scale height of the H I layer (Heiles 1990). Oey & Clarke (1997) note, though, that the distributions do not show a limiting radius due to the disk scale height. The same is true in our sample where the cutoff radius is larger than the H I scale height. We suggest that this may be due to magnetic fields. Simulations of supernovae expanding in magnetized regions show that the remnants tend to elongate along the magnetic field lines (Insertis & Rees 1991; Rozyczka & Tenorio-Tagle 1995). The magnetic fields initially restrict expansion out of the plane, allowing the SNR to expand further along the plane. Tomisaka (1998) showed that the same effect is true for superbubbles expanding in a magnetic field. The magnetic field lying parallel to the plane provides pressure that confines shells, so that they grow larger along the plane than perpendicular to the plane. This allows shells' major axis length in the plane to exceed the scale height of the disk, while radii perpendicular to the plane remain under the scale height. Of course, as a shell continues to expand the radius perpendicular to the plane can reach a height where the density gradient becomes significant and the shell then grows out of the plane. Additionally, sequential star formation may be confined to the plane. Therefore, one might expect the majority of large H I shells to be elongated along the plane. It is unclear whether this effect is seen explicitly in our catalog; the most distinct examples are GSH 304-00-12 and GSH 337-02-27.

The distribution of expansion velocities is shown in Fig. 5.17. Only SGPS shells and those with tabulated expansion velocities from Heiles (1979) are included in this plot. This sample is extremely small, so we do not attempt a similar power-law fit. We believe that the lower cutoff is a selection effect. SGPS shells, by definition, have expansion velocities over 2 km s^{-1}. The Heiles (1979) data have 2 km s^{-1} channels that are spaced 4 km s^{-1} apart, so a shell observed over more than two channels must have an expansion velocity of at least $\sim$ 6 km s^{-1}. The nature of the upper cutoff is less clear. There is no natural bias in our data against shells with large expansion velocities. And yet, our cutoff expansion velocity of $v \sim 25$ km s^{-1} agrees well with that found in the SMC, M31 and M33 (Stanimirović et al. 1999). We note, however, that for a shell powered by a typical OB association - such as Cen OB1 in Chapter 4 - the expansion velocity will only be in excess of 30 km s^{-1} for the 1 Myr of the shell's expansion. At 1 Myr a typical shell is only 10-20 pc is radius. A shell that small would have been below the resolution limit of the external galaxy shell catalogs and below the angular size selection limit of the SGPS catalog for all shells at distances greater than 1.5 kpc. We expect, then, that an expanded SGPS catalog, including high resolution ATCA data will increase the expansion velocity cutoff.

Several authors have tried to correlate OB associations with H I shells, both in the Milky Way (Cowie et al. 1981; Heiles 1984) and external galaxies (e.g. M31, M33,

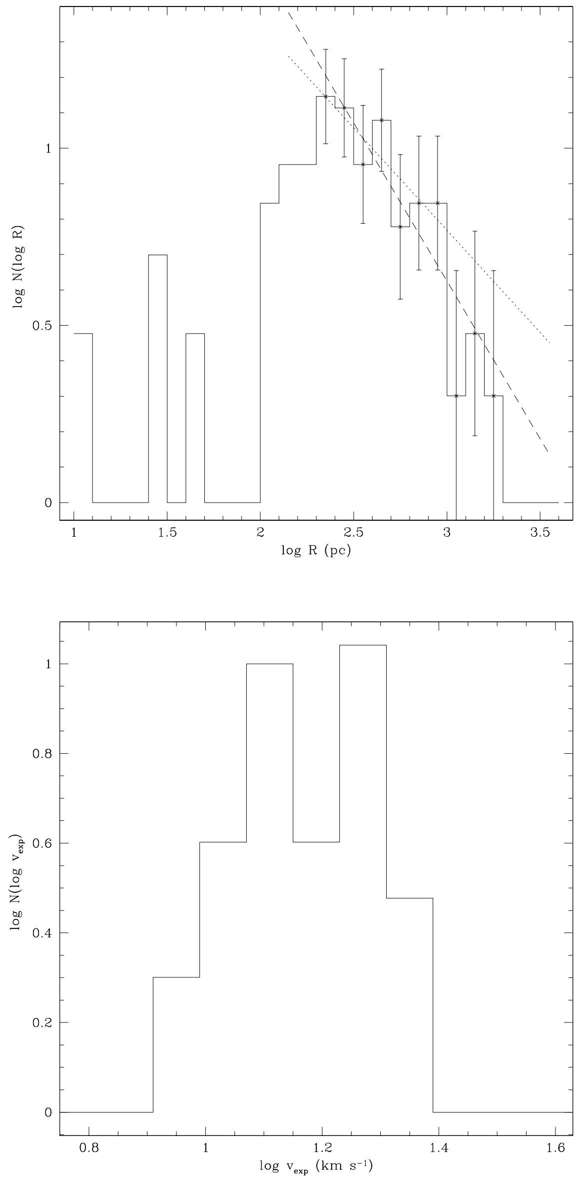

Figure 5.17: Histograms of H I shell radii (top) and expansion velocities (bottom). The shells included are the seventeen new SGPS shells and all shells (expanding and stationary for the radius histogram, only expanding for the velocity histogram) from Heiles (1979, 1984). The shells are binned logarithmically to allow for a least-squares fit to the distribution. For the radius histogram the distribution is fit with $\log N(\log R) = \gamma_r \log R + \delta_r$, which gives the power-law slope, $N(R) \propto R^{-\alpha_r}$, where $\alpha_r = 1 - \gamma_r$.

LMC; Brinks & Bajaja 1986; Deul & den Hartog 1990; Kim 1998). In the Milky Way these attempts are hampered by extinction towards distant stars and as a result, few OB associations have been identified beyond $\gtrsim$ 2.5 kpc (Humphreys 1978; Mel'Nik & Efremov 1995). Catalogs of H I shells, by contrast, contain many distant shells which makes it difficult to perform an accurate correlation analysis. Furthermore, nearby shells in the inner Galaxy, which may be correlated with OB associations, are very difficult to detect because of distance ambiguities, large gas filling factors, and extremely large angular sizes. In external galaxies extinction is less of a problem and many OB association-H I shell correlations have been identified. Deul & den Hartog (1990) found that for H I shells in M33 smaller shells ($R < 100$ pc) correlate well with OB associations but larger shells ($R > 250$ pc) tend to show an anti-correlation, with star formation more concentrated on the shell walls. In the LMC, where the shell sample is larger, the correlation begins to break down and many shells are identified without OB associations or ionized gas (Kim 1998). In our sample we find few correlations with OB associations, only GSH 305+01-24 and GSH 337+00-25 likely belong to associations. We searched for H I shells at the positions of all survey area OB associations cataloged by Humphreys (1978) and found no new shells. We also examined H II regions and H I shells and found that H II regions were typically located exterior to the shells.

5.5 H I Shells at High Resolution

This chapter has so far only used Parkes data, the inclusion of the full ATCA mosaics opens a new window to the study of H I shells. The high resolution data reveal many characteristics not visible in low resolution surveys. In particular, high resolution allows us to study the development of instabilities in H I shells and chimneys. With these data we can test theories of H I chimney formation and the destruction of H I shells by turbulent motions in the ISM.

Instabilities of many varieties are expected in H I shells. Recent three-dimensional simulations of multiple supernovae in the Galactic disk show shells that develop Rayleigh-Taylor (R-T) instabilities as they expand vertically (de Avillez 2000). At the interface between the dense thin and diffuse thick H I disks, simulated shells fragment and release their hot interior gas to the halo through narrow channels. These models predict that fragmentation produces H I sheets and clouds on scales of 5-100 pc. These should be readily detectable with the complete SGPS data. R-T instabilities are also expected at the interface of two interacting shells, of which this catalog contains several examples. Breitschwerdt et al. (2000) explored the case of two interacting shells, finding that where the pressure of one shell dominates the other, R-T instabilities will develop. They simulated the interaction of the Local Bubble and the Loop I superbubble, taking into account the magnetic field characteristics of the region and found that instabilities develop with characteristic sizes of the width of the shell wall.

5.5.1 Shell walls

With complete H I surveys of the LMC and SMC (Kim et al. 1998; Stanimirović et al. 1999) it has become clear that the H I morphology of these galaxies is dominated by large shells, resulting in a filamentary structure. The weak correlation between H I shells and OB associations in the LMC, coupled with the number of extremely large shells has again raised the question of whether or not these structures are formed from stellar winds and supernovae. In particular, it is difficult to envisage how star formation could have been so active as to form as the number of observed shells in timescales as short as 5-30 Myr. As an alternative explanation two-dimensional hydrodynamic models by Wada & Norman (1999) have shown that a thermally and gravitationally unstable disk can generate structures that resemble shells with dense clumps and filaments surrounding a hot gas interior. Wada et al. (2000) expanded on these simulations with further models of a two-dimensional LMC-type galaxy. They modeled the galaxy both including star formation (SF models) and excluding star formation (NSF model).

The porous, filamentary morphology was, in their simulations, attained without intense star formation. They found that star formation tends to disrupt formation of large-scale (> 1 kpc) cavities in the inner regions of the galaxy. The velocity structure of their cavities mimics the behavior of expanding supershells. We note, though, that these simulations are two-dimensional and therefore do not test whether the full three-dimensional structure of the shells can also be re-created without star formation. These simulations raise the question, though, of how to distinguish between structures formed by the interaction of stars with the ISM and those formed from gravitational instabilities.

Preliminary evidence from the SGPS suggests that the shell walls may help us to determine the nature of shell-like structures. Using the full resolution SGPS we have examined seven shells identified in the Parkes data: GSH 255-00+52, GSH 256+00+63, GSH 263+00+47, GSH 277+0+36, GSH 280+0+59, GSH 297-00+72, and GSH 319-01+13. All seven of these shells have thin walls, with varying degrees of structural integrity. In all cases the shell walls are $\sim 5 - 15$ pc wide or 2-4% of the shell radius. Of these shells, GSH 256+00+63 (Fig. 5.20), GSH 277+00+36 (Fig. 5.21), and GSH 297-00+72 (Fig. 5.18) have the most clearly defined, strong walls. Images of the shells show very sharp interior edges on the shell walls. Towards the exterior, the walls decay more gradually into the ambient ISM. This is confirmed in profiles across the shell walls. An example profile is shown in Fig. 5.19; this is a slice across the edge of GSH 297-00+72 at $b = 0\overset{\circ}{.}556$. The strong peak at $l = 299^\circ$ is the wall of the shell. As marked, the H I void is towards lower longitudes and the exterior ISM is at $l \gtrsim 299\overset{\circ}{.}5$. We found similar profiles for all shells examined. Each included the same details: a very steep wall towards the shell interior and a more gradual slope on the exterior of the wall. The sharp profile is an expected characteristic of a wall swept-up by a blast wave. Because the filaments suggested by Wada et al. (2000) are not formed by compression it is unlikely that they would exhibit the same asymmetric profile. Therefore, the

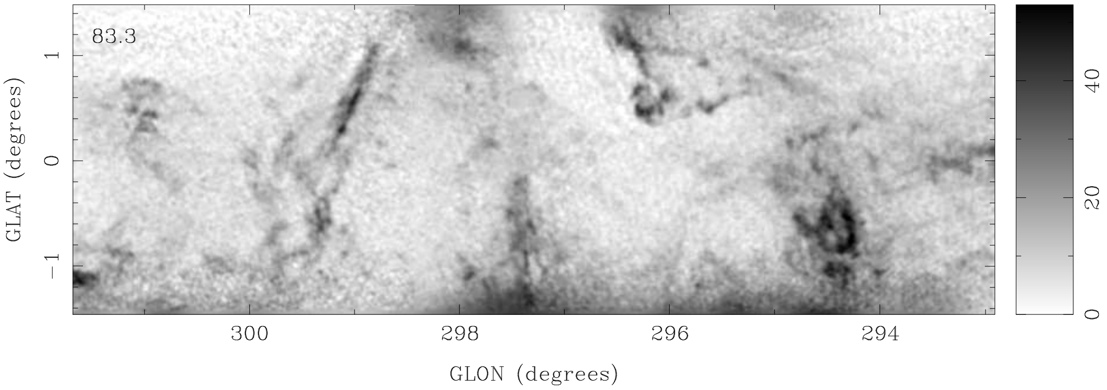

Figure 5.18: Grey scale image of GSH 297-00+72, including both Parkes and ATCA data. The grey-scale is linear from 5 to 50 K, as shown in the wedge at the right. The image shows the incomplete, narrow wall separating the two halves of the shell.

spatial structure of the shell may allow us to distinguish shells formed by gravitational instabilities from pressure driven shells.

Another point of interest is the relationship of H I shells to the spatial power spectrum. Measurements of the spatial power spectrum (SPS) show a power law behavior covering scales of a few hundred parsecs to a few parsecs. Studies of the H I SPS in the SGPS and SMC (Dickey et al. 2001; Stanimirović et al. 1999) show a clear logarithmic power-law, with a slope that is consistent with a Kolmogorov energy cascade (see Lazarian & Pogosyan 2000; Goldman 2000). Goldman (2000) suggests that the largest turbulent eddies may be kiloparsecs in scale, possibly powered by Galactic differential rotation. This implies that there may be stochastic fluctuations in the ISM on large scales that are distinctly different from deterministic structures on similar scales, such as shells. Can we distinguish these fluctuations from true, deterministic H I shells? Alternately, it has been suggested that deterministic structures, such as H I shells, are powering a cascade of energy in the Galaxy (Spangler 2001). One might expect then, that an examination of the SPS of a region containing a large shell would show a break from a smooth power-law at the size scale of the shell. To test this we calculated the

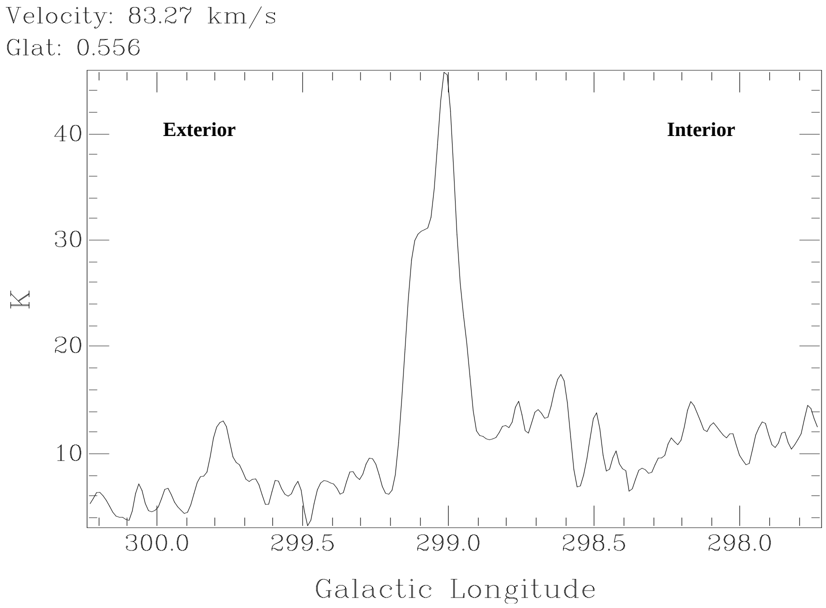

Figure 5.19: Profile across the edge of GSH 297-00+72 at $b = 0\overset{\circ}{.}556$. The strong peak at $l = 299°$ is the wall of the shell. The H I void is towards lower longitudes and marked as "Interior" and the exterior ISM is at $l \gtrsim 299\overset{\circ}{.}5$.

SPS of the area containing the large, intact shell GSH 277+00+36, as well as gas surrounding the shell. The SPS, however, reveals a clear power law with a slope of −3, and no breaks at any spatial scales sampled by the SGPS. This seems to suggest that either the SPS as a tool is very insensitive to deterministic structures or that the shell is part of the largest structures feeding the energy cascade. Future simulations of turbulent ISM structure, such as those by Vazquez-Semadeni & Avila-Reese (2000), may be the only way to determine which scenario is correct.

5.5.2 Specific Examples

GSH 256+00+63

High resolution observations of the first example shell, GSH 256+00+63, reveal a direct association with an H II region on the right edge of the shell. Fig. 5.20 is grey scale image of six velocity channels centered at $v = +64$ km s^{-1}, including the main shell, GSH 256+00+63, and a second, weaker shell to the right surrounding the H II region G254.676+0.229 (Caswell & Haynes 1987). The second shell is most noticeable close to the H II region (seen in absorption as a small, white dot) at the wall separating the shells. Extending from the H II region into GSH 256+00+63 is a thin filament. At the distance of this shell, the filament is physically very narrow, $\sim$ 5 pc in some places, and extends for more than 100 pc. If the shell were filled with molecular gas then the H I filament might actually be a photo-dissociation jet from the H II region. In this scenario an outflow from the H II region into molecular gas interior to the H I shell would photo-dissociate the molecules, leaving an H I feature. However, examination of CO data from Dame et al. (1987) reveals no CO at this position. The filament is more likely the result of an instability due to the pressure difference between the large shell and the H II region. As mentioned above, Breitschwerdt et al. (2000) have shown that Rayleigh-Taylor instabilities can develop at the interface of two shells due to the pressure difference between the adjacent regions. The filament may therefore be a Rayleigh-Taylor finger extending into the shell. Further study of this object will allow us to determine if this is indeed a R-T finger and therefore derive the pressures of the shells.

GSH 277+00+36

GSH 277+00+36 at high resolution also contains a wealth of small-scale structure. Fig. 5.21 shows two velocity planes of the shell at $v = 36.3$ km s^{-1} and $v = 45.3$ km s^{-1}. This chimney is ideal to commence a high-resolution study of instabilities in chimney formation. The high resolution images reveal small scale ($\sim$ 6 $-$ 10 pc) structures at the edges of the shells and very thin walls ($\sim$ 15 $-$ 20 pc; see Figure 5.21). The $v = 36$ km s^{-1} plane, in particular, shows a small shell embedded in the bottom left edge of the main H I void. As seen in Chapter 3 (see Fig. 3.4), GSH 277+00+36 is not a cohesive, conical outflowing chimney. Instead it appears to agree with the de Avillez

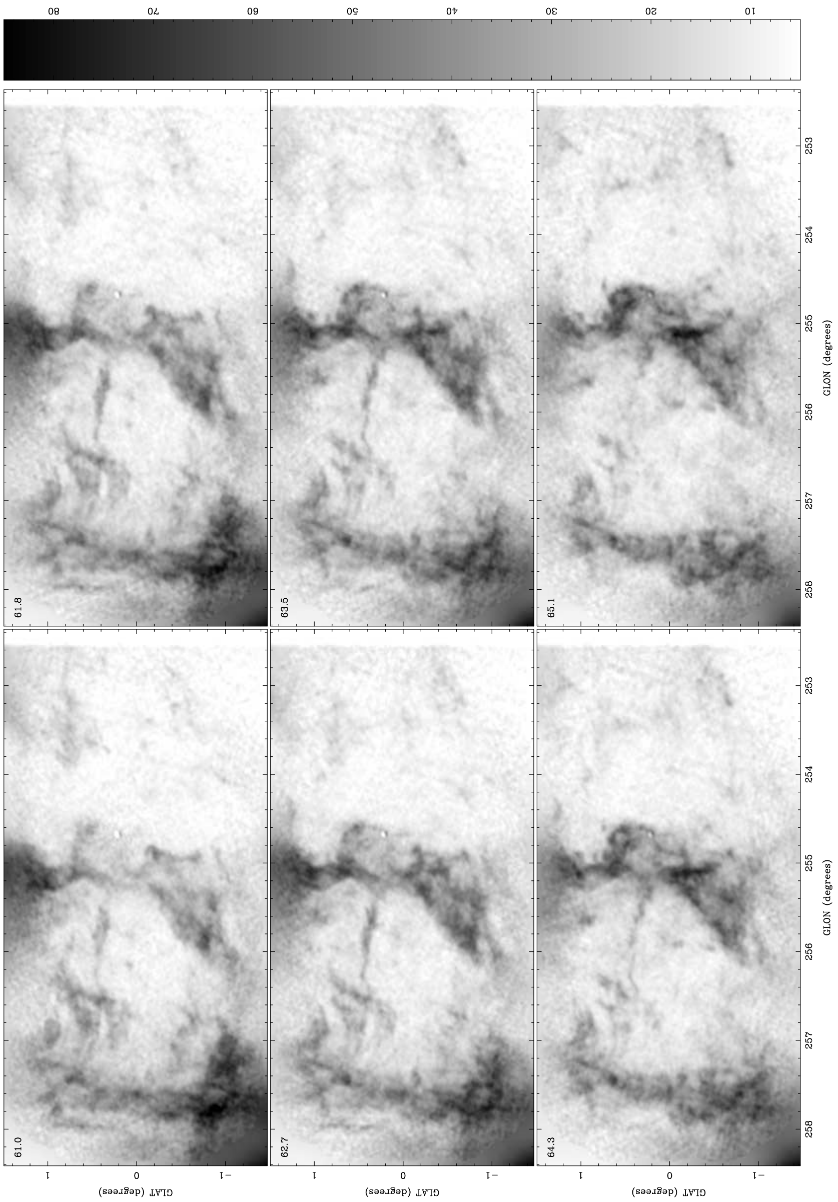

Figure 5.20: Grey scale channel images of GSH 256+00+63. Six velocity channels separated by 0.82 km s^{-1} are shown, centered on v = 62.7 km s^{-1}. The grey-scale is linear from 5 to 90 K, as shown in the wedge at the right. GSH 256+00+63 is the large structure, while the small, half-shell to the right is associated with the H II region 254.676+0.229.

(2000) simulations that shows supershell that fragmented at the edge of the thick disk, creating narrow worm-like conduits out both sides of the plane. This suggestion is supported by the small-scale structure in the upper right-hand corner of the shell wall where it appears to be developing instabilities. The instabilities are potentially very interesting as probes of the physical conditions relating to break-out.

We expect that the chimney walls and interiors will have many small scale features that may demonstrate how chimneys supply gas to the halo and how they evolve. This chimney also lies on the trailing edge of the Carina spiral arm where it appears to have expanded into the interarm region. In Chapter 3 we suggested that shells may break into interarm regions in a process that is similar to the break-out above the plane. If this is true, this shell offers an unique opportunity to study both break-out processes in the same object. Unfortunately, the upper latitude extensions of this shell are not covered by the current ATCA observations and will therefore require further observations. These observations will be completed in the next year.

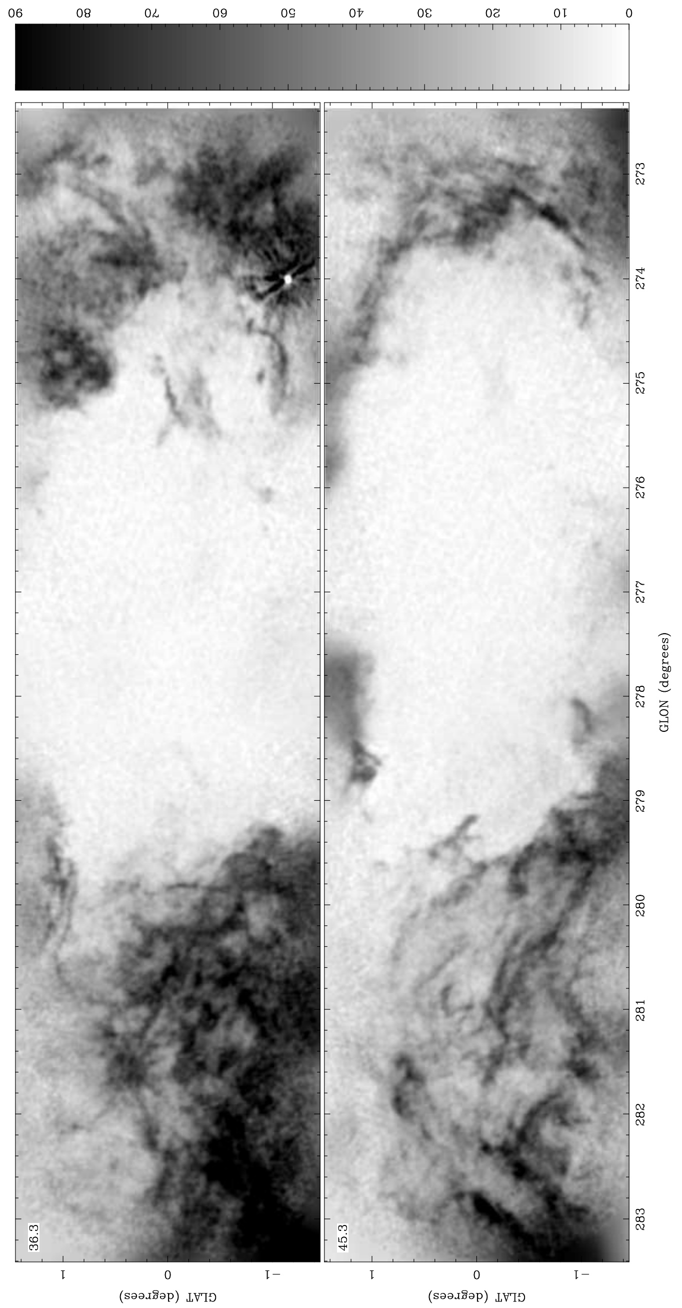

Figure 5.21: GSH 277+0+36 at $2'$ resolution. The data shown here are combined ATCA and Parkes data from the SGPS. The top image is at the shell center, $v = 36.3$ km s^{-1}. The bottom image is at $v = 45.3$ km s^{-1}. The greyscale in both images is linear and runs from 0 K to 90 K as shown in the wedge at the right. These images reveal small scale structure along the shell walls, in addition to a very thin shell wall.